This manuscript is titled **'Ocean-bottom Seismic Interferometry in Coupled Acoustic-Elastic Media'** with authors: **Adesh Pandey** (adesh0805@gmail.com)**, Jeffrey Shragge** (jshragge@gmail.com)**, Ashish Kumar** (akumar1@mines.edu) and **Aaron J. Girard** (aaron.j.girard@gmail.com)**.** It has been submitted for review in **Geophysics.**

Please note that while this manuscript is undergoing peer-review, it has not been accepted for publication at the time of submission to EarthArxiv. Subsequent versions of the manuscript may have slightly different content. If accepted, the final version of this manuscript will be available via the 'Peer-reviewed Publication DOI' link on the EarthArxiv posting page. Please feel free to contact any authors with feedback.

Scholte-wave Adjoint Tomography for Building Low-frequency, Offshore Shear-wave Velocity Models

Adesh Pandey[1*] Jeffrey Shragge[1] Ashish Kumar[1]
Aaron J. Girard[1]

February 9, 2026

[1]Center for Wave Phenomena, Department of Geophysics, Colorado School of Mines, 901 17th St., Suite 400, Golden, CO, 80401, USA

Abstract

Field observations have shown that low-frequency (sub-1 Hz) Scholte waves retrieved from ocean-bottom node (OBN) data are strongly influenced by large-scale velocity heterogeneities such as salt bodies, underscoring their potential for offshore model building. However, procedures for translating this sensitivity into reliable subsurface velocity models remains poorly understood. Motivated by these observations, we investigate the feasibility of using low-frequency Scholte-wave travel-time adjoint tomography to construct long-wavelength offshore shear-wave velocity (V_S) models suitable as starting models for elastic full-waveform inversion (E-FWI). Using a 2-D synthetic model that includes an ocean layer and a realistic, laterally variable salt body, we simulate empirical Green's functions recorded by dense OBN arrays and compute travel-time misfit kernels for both background and true V_P–ρ parameterizations, starting from a background V_S model with large ($\sim$50%) perturbations relative to the true model. Fréchet-kernel analyses confirm that Scholte waves are dominantly sensitive to V_S variations, with only weak indirect dependence on V_P and ρ. The tomographic inversion employs a multimodal strategy that combines fundamental and higher-order Scholte modes within a hierarchical frequency-stepping scheme. Even when all parameters are initialized from the background, the inversion recovers the overall salt geometry and V_S structure reasonably well, demonstrating that large-scale V_S recovery is achievable without the true V_P–ρ contrasts. Incorporating the correct V_P and ρ distributions further improves depth focusing and reduces parameter trade-offs, yielding enhanced vertical resolution. The recovered V_S models reproduce the long-wavelength salt geometry, with intermediate-depth velocities estimated within $\sim$10% of the true values,

*Corresponding author: adesh0805@gmail.com

although structures deeper than ∼6 km and shallower than ∼2 km remain underconstrained within the tested 0.10–0.45 Hz band. These results demonstrate that low-frequency Scholte-wave adjoint tomography provides a robust, practical pathway for constructing reliable long-wavelength V_S models and a physically consistent foundation for initializing E-FWI in complex offshore environments.

1 Introduction

Elastic velocity model building is a critical step for producing high-resolution, geologically meaningful subsurface images. Among the available methods, elastic full-waveform inversion (E-FWI) is widely recognized as one of the most powerful approaches for recovering detailed and accurate Earth models. In contrast, more computationally efficient acoustic FWI analyses neglect the elastic nature of wave propagation and fail to account for elastic wave phenomena including P–S mode conversions and amplitude variation with offset (AVO), both of which are controlled by contrasts in the shear modulus μ. As a result, the acoustic assumption limits the ability to reproduce seismic responses that are physically consistent with the true elastic behavior of the subsurface as expressed in observed field data. Accurately characterizing subsurface S-wave velocities (V_S) is therefore crucial for recovering the full elastic behavior of the Earth; however, fully achieving this goal remains challenging and current model building practice continues to limit the effectiveness of physics–based elastic imaging in practice.

The success of an iterative E-FWI analysis also depends on starting from an accurate long-wavelength velocity model to avoid cycle skipping and convergence to an incorrect model solution [5, 58]. To mitigate this, E-FWI is typically implemented in a multiscale fashion, starting with lower-frequency data and progressively introducing higher frequencies once the analysis with lower-frequency data has constrained larger-scale velocity model structure [50, 37]. In marine active-source acquisition, this multiscale strategy is limited by the frequency content of air-gun arrays, which struggle to generate coherent energy below 2.0 Hz in any given shot gather. This "frequency floor" restricts the ability to recover the long-wavelength velocity trends required for stable elastic inversion. Although specialized low-frequency sources can partially extend this range [14], their deployment remains costly and logistically complex. As a result, there is growing interest in leveraging naturally occurring ambient seismic wavefields, which are intrinsically rich in low-frequency energy well below the active-source cutoff frequency [e.g., 7, 12, 2, 41].

Continuous recordings on dense ocean-bottom arrays have demonstrated that ambient seismic interferometry can extract coherent signals between 0.05–2.00 Hz [53, 52, 7] that are sensitive to large-contrast subsurface velocity heterogeneities [12, 21, 20]. These wavefields are dominated by dispersive wave modes, most prominently Scholte surface and guided P waves. With the growing deployment of ocean-bottom seismometers (OBSs), cables (OBCs), nodes (OBNs),

and more recently, distributed acoustic sensing (DAS) arrays [10, 51], there is now unprecedented access to densely sampled long-duration seafloor recordings. Although originally designed for active-source surveys, the datasets from typical ocean-bottom sensor deployments also capture months of ambient low-frequency wavefield data that can be exploited to recover the long-wavelength elastic structure needed to initialize E-FWI.

Viewed within the broader seismic spectrum, high-frequency surface waves (i.e., $f \geq 2.0$ Hz) provide a direct link to V_S models in the shallow subsurface and are widely used in one-dimensional (1-D) dispersion inversion or MASW analyses [64, 63, 60, 61]. In contrast, the global seismological community routinely exploits much lower frequencies (i.e., $f \leq 0.05$ Hz) in Rayleigh-wave-based regional and global imaging to probe lithospheric and upper-mantle structures [e.g., 29, 16]. Between these two regimes (i.e., $0.05 < f < 2.0$ Hz) lies an underexploited "frequency gap", made available through naturally occurring secondary microseism energy and potentially valuable for exploration-scale imaging. Recent advances in ocean-bottom ambient-seismic interferometry have demonstrated that this intermediate-frequency range can be effectively used in offshore settings through the recovery of sub-1.0 Hz Scholte-wave energy that is sensitive to deep sedimentary and salt structures [13, 21, 41]. These low-frequency surface waves, observed on virtual shot gathers (VSGs)—generated through seismic interferometry of ambient energy recorded by ocean-bottom sensors—can penetrate several kilometers below the seafloor (e.g., 4–5 km), making them particularly attractive for long-wavelength offshore velocity model building.

Field observations support this potential: [21] analyzed ambient virtual shot gathers (VSGs) from dense OBN deployments and demonstrated a clear imprint of subsurface salt bodies on propagating sub-1.0 Hz Scholte waves. Snapshots of wave propagation (Figures 10–12 in that study) show that shallow-propagating acoustic waves (guided P) are unaffected by the deeper structure; however, as low-frequency Scholte-wave energy reaches salt bodies, wavefronts exhibit distortion and clearly propagate at faster velocities due to the higher-velocity salt. These effects persist across multiple propagation lags throughout the VSG volume, highlighting the strong sensitivity of low-frequency Scholte waves to lateral and vertical velocity contrasts. Importantly, these signatures were observed directly in ambient field data without relying on active-source constraints, and provide compelling evidence that low-frequency Scholte waves carry information potentially useful for estimating large-scale, long-wavelength V_S structures in realistic offshore settings.

Traditionally, surface-wave dispersion analysis has been used to estimate one-dimensional (1-D) shear-velocity profiles. For instance, [45] introduced the multichannel analysis of surface waves (MASW) method to interpret and invert Rayleigh, Love, and Scholte dispersion curves for 1-D V_S structure at representative array locations. Although such inversions provide valuable local constraints, they inherently assume lateral homogeneity and thus cannot capture the complex spatial variability characteristic of offshore environments. To overcome this limitation, our objective is to move beyond 1-D approaches and construct 2-D

and 3-D V_S models using full surface-wave waveforms.

Motivated by these field observations and methodological limitations, this study focuses on low-frequency (sub-1.0 Hz) Scholte-wave adjoint travel-time tomography as a pathway for building long-wavelength V_S models suitable for initializing E-FWI in the typical exploration seismic inversion frequency bands (i.e., $\sim$ 2.0-20.0 Hz). In the case of ocean-bottom sensor data, these low-frequency surface waves are generally retrieved through seismic interferometry on long-time ambient wavefield recordings [e.g., 52, 40, 21, 20]. While ambient wavefield inversion approaches that directly model [43, 44] and invert ambient cross-correlations for velocity structure and ambient source distribution have been proposed [48, 47, 65], the present study focuses on isolating the structural sensitivity of Scholte waves by using empirical Green's function (EGF) representations of ambient cross-correlations extracted from OBN records. This choice enables a systematic evaluation of how multi-modal Scholte-wave phases constrain long-wavelength shear velocity structures, independent of uncertainties associated with ambient source distribution modeling and inversion. Consequently, the motivation remains on surface-wave tomography approaches that emphasize phase information while avoiding reliance on amplitude, since the arrival phases in the EGFs have been shown to remain consistent with those in true Green's functions under ideal ambient source characteristics and distribution conditions [62, 22]. Amplitude information, though, is less reliable due to the approximations inherent in interferometry for practical cases [62, 26] as well as the linear and nonlinear processing of ambient data used to generate VSGs, both of which introduce significant amplitude distortions between EGFs and Green's functions [62, 19]. Consequently, the motivation remains on surface-wave tomography approaches that emphasize phase information while avoiding reliance on amplitude, since the arrival phases in the EGFs have been shown to remain consistent with those found in true Green's functions under ideal ambient source characteristics and distribution conditions.

In the following sections, we first review the theoretical framework of adjoint travel-time tomography, including the formulation of misfit functions, adjoint sources, and sensitivity kernels. We then describe the construction of a 2-D synthetic offshore model containing a realistic salt body and outline the survey geometry used in our numerical experiments. Using this setup, we illustrate the sensitivity of Scholte waves to variations in P-wave velocity (V_P), shear-wave velocity (V_S), and density (ρ), as well as the depth-dependent contributions of different frequencies and modal components to model updates. Building on these insights, we implement a staged multi-modal tomographic inversion strategy and evaluate its ability to recover long-wavelength V_S structure. Finally, we discuss the practical and broader implications of our findings for offshore velocity model building and the initialization of E-FWI.

2 Theory of Adjoint Tomography

The theory of adjoint tomography has been well covered in the existing seismic inversion literature [57, 18, 34, 32]. For completeness, we summarize the key elements of adjoint-based tomographic inversion, including the roles played by event misfit kernels and gradient formulations in tomographic inversion frameworks. Throughout this work, we refer to a source as an event.

Within a general seismic inversion framework, the observed seismograms, $\mathbf{d}(\mathbf{x}_r, \mathbf{x}_s, t)$, recorded at receiver locations $\mathbf{x}_r$ from sources excited at location $\mathbf{x}_s$, are compared with their synthetic counterparts, $\mathbf{s}(\mathbf{x}_r, \mathbf{x}_s, \mathbf{m}, t)$, generated by forward modeling the injected source energy through a parameterized Earth model $\mathbf{m}$. The model $\mathbf{m}$ is subsequently updated in an iterative fashion to minimize discrepancies between observed and synthetic data. This discrepancy is quantified by a misfit function, which acts as the objective function of the optimization problem. Denoting the misfit of an Earth model by $\chi(\mathbf{m})$, we may write

$$\chi(\mathbf{m}) = \sum_{s=1}^{N_s} \sum_{r=1}^{N_r} \int_{t_0}^{t_1} g(\mathbf{x}_r, \mathbf{x}_s, t, \mathbf{m})\, \mathrm{d}t, \tag{1}$$

where N_s and N_r denote the number of sources and receivers, respectively; $t \in [t_0, t_1]$ specifies the time interval of the analysis window; and $g(\mathbf{x}_r, \mathbf{x}_s, t, \mathbf{m})$ represents the chosen misfit measure (e.g., waveform difference, cross-correlation travel time) between the observed and synthetic data.

The gradient of the objective function $\chi(\mathbf{m})$ with respect to the reference model $\mathbf{m}$ is expressed as [57]:

$$\partial\chi(\mathbf{m}) = \int_V K_m(\mathbf{x})\, \partial \ln \mathbf{m}(\mathbf{x})\, \mathrm{d}^3\mathbf{x}, \tag{2}$$

where V denotes the Earth volumetric model space; $\mathbf{x} \in V$; and $K_m(\mathbf{x})$ is the Fréchet kernels, or misfit sensitivity kernels, defined for fractional perturbations of model parameters (i.e., $\partial \ln \mathbf{m}$). Within the adjoint-method framework [57, 33], these kernels are constructed from the interaction of the forward wavefield emitted by the source and the adjoint wavefield generated by time-reversed adjoint sources at receiver locations. Comprehensive derivations of adjoint sources and sensitivity kernels for different seismic parameters are provided in [57], [34], and [17].

There are several approaches to derive model updates using event kernels [38]. Here, we adopt an update that is linearly proportional to the sum of event kernels. Consider the quadratic Taylor expansion of the misfit function [56] in the vicinity of $\mathbf{m}$:

$$\chi(\mathbf{m} + \delta\mathbf{m}) = \chi(\mathbf{m}) + \mathbf{g}(\mathbf{m})^T \delta\mathbf{m} + \tfrac{1}{2}\, \delta\mathbf{m}^T \mathbf{H}(\mathbf{m}) \delta\mathbf{m} + \mathcal{O}\big(\|\delta\mathbf{m}\|^3\big), \tag{3}$$

where $\mathbf{g}(\mathbf{m})$ is the gradient

$$\mathbf{g}(\mathbf{m}) = \left.\frac{\partial\chi(\mathbf{m})}{\partial\mathbf{m}}\right|_{\mathbf{m}}, \tag{4}$$

and the Hessian $\mathbf{H}(\mathbf{m})$ is the curvature

$$\mathbf{H}(\mathbf{m}) = \left.\frac{\partial^2 \chi(\mathbf{m})}{\partial \mathbf{m}^2}\right|_{\mathbf{m}}, \tag{5}$$

of the misfit function with respect to model parameters $\mathbf{m}$. The gradient of equation 3 evaluated at the perturbed model $\mathbf{m} + \delta\mathbf{m}$ is then given by

$$\left.\frac{\partial \chi(\mathbf{m}')}{\partial \mathbf{m}'}\right|_{\mathbf{m}'=\mathbf{m}+\delta\mathbf{m}} = \mathbf{g}(\mathbf{m}+\delta\mathbf{m}) \approx \mathbf{g}(\mathbf{m}) + \mathbf{H}(\mathbf{m})\,\delta\mathbf{m}, \tag{6}$$

which is set to zero to obtain the nearest minimum of $\chi(\mathbf{m})$ in equation 1. The model perturbation $\delta\mathbf{m}$ satisfying this condition is

$$\delta\mathbf{m} = -\mathbf{H}^{-1}(\mathbf{m})\mathbf{g}(\mathbf{m}). \tag{7}$$

Here, the gradient $\mathbf{g}(\mathbf{m})$ can be said to be "preconditioned" by the generalized inverse of the Hessian operator $\mathbf{H}^{-1}(\mathbf{m})$. In practice, equation 7 forms the basis of an iterative optimization scheme in which the model parameters are successively updated along the search direction defined by $\delta\mathbf{m}$ until convergence is achieved. Within the optimization framework, an updated model at the $j+1$ iteration, $\mathbf{m}_{j+1}$, is expressed as

$$\mathbf{m}_{j+1} = \mathbf{m}_j + \alpha\,\delta\mathbf{m}_j, \tag{8}$$

where $\mathbf{m}_j$ is the model at the existing iteration, α is the step length controlling the extent of the update, and $\delta\mathbf{m}_j$ is the model update direction. The step length α is typically determined using a line search in conjunction with a gradient-based optimization algorithm (e.g., nonlinear conjugate gradient or limited-memory Broyden–Fletcher–Goldfarb–Shanno (L-BFGS)) [31, 42, 58].

Model updates can be computed either with or without the Hessian, $\mathbf{H}$. In classical travel-time tomography, both the gradient $\mathbf{g}$ and Hessian $\mathbf{H}$ of the misfit function are typically obtainable, allowing the model update $\delta\mathbf{m}$ to be computed using equation 7. In scenarios involving complex heterogeneous models and large-scale problem dimensionality, computing the gradient is generally feasible; however, evaluating the full Hessian operator or individual kernels becomes impractical due to prohibitive computational and storage costs. In such cases, various approximate preconditioners (e.g., diagonal Hessian, Gauss–Newton, model-dependent scaling factors) can be applied to the gradient to improve convergence [38]. In the absence of computed Hessian information, the misfit function can still be minimized iteratively by updating the model along the negative gradient direction,

$$\delta\mathbf{m} \propto -\,\mathbf{g}(\mathbf{m}). \tag{9}$$

2.1 Misfit function and sensitivity kernels

The choice of misfit function determines both the type of structural information that can be extracted from the data and the overall stability of the inversion. Various misfit functions emphasize different aspects of the waveforms:

some are more sensitive to long-wavelength structure, while others highlight fine-scale details. There is an inherent trade-off between resolution and stability—misfit functions that promote sensitivity to small-scale structure can resolve sharper features but are generally more susceptible to noise, cycle skipping, and erroneous convergence to local minima [66]. Consequently, the choice of misfit function must be guided by the nature of the available data and the analysis objective. In the case of ambient seismic cross-correlations, amplitude measurements are generally unreliable; therefore, it is preferable to use travel-time-based misfit functions that are still capable of providing robust constraints on the large-scale elastic structure. A comprehensive review of different misfit functions for adjoint full waveform inversion in seismology can be found in [4] and [59].

In travel-time tomography, the misfit function measures the squared travel-time difference for a selected seismic phase [57, 55, 4]:

$$\begin{aligned}\chi(\mathbf{m}) &= \frac{1}{2}\sum_{s=1}^{N_s}\sum_{r=1}^{N_r}\left[T^{\text{obs}}(\mathbf{x}_s,\mathbf{x}_r) - T(\mathbf{x}_s,\mathbf{x}_r,\mathbf{m})\right]^2 \\ &= \frac{1}{2}\sum_{s=1}^{N_s}\sum_{r=1}^{N_r}\delta T(\mathbf{x}_s,\mathbf{x}_r,\mathbf{m})^2,\end{aligned} \tag{10}$$

where $T^{\text{obs}}(\mathbf{x}_s,\mathbf{x}_r)$ denotes the observed traveltime of a selected phase for the s-th source and r-th receiver pair located at $\mathbf{x}_s$ and $\mathbf{x}_r$, respectively; $T(\mathbf{x}_s,\mathbf{x}_r,\mathbf{m})$ is the corresponding predicted traveltime from the current model $\mathbf{m}$; and N_s and N_r are the total number of sources and receivers, respectively. For multiple phases, the total misfit is obtained by summing contributions from each phase. For notational compactness, we omit the explicit phase dependence of the misfit function below.

In the context of tomographic inversion, the travel-time misfit for an isolated phase between s-th source and r-th receiver pair is measured by cross-correlating the observed and predicted waveforms within a time window containing the selected phase,

$$\delta T(\mathbf{x}_s,\mathbf{x}_r,\mathbf{m}) = \arg\max_{\Delta t}\int_0^T w(\mathbf{x}_s,\mathbf{x}_r,t)\,\mathbf{d}(\mathbf{x}_s,\mathbf{x}_r,t)\,\mathbf{s}(\mathbf{x}_s,\mathbf{x}_r,t+\Delta t,\,\mathbf{m})\,\mathrm{d}t, \tag{11}$$

where $\mathbf{d}(\mathbf{x}_s,\mathbf{x}_r,t)$ and $\mathbf{s}(\mathbf{x}_s,\mathbf{x}_r,t,\mathbf{m})$ denote the observed and predicted displacement seismograms, respectively; $w(\mathbf{x}_s,\mathbf{x}_r,t)$ is a windowing operator that isolates the chosen phase; and Δt is the time shift that maximizes the cross-correlation within the analysis interval $t \in [0,T]$. A negative Δt indicates that the synthetic waveform is delayed, or lags, behind the observed waveform, whereas a positive Δt implies the converse.

This definition of travel-time misfit leads to the travel-time adjoint source [57, 55, 4]:

$$f^\dagger(\mathbf{x}_r,t) = -\sum_{s=1}^{N_s}\frac{\delta T(\mathbf{x}_s,\mathbf{x}_r)\,w(\mathbf{x}_s,\mathbf{x}_r,T-t)\;\dot{\mathbf{s}}(\mathbf{x}_s,\mathbf{x}_r,T-t)}{N(\mathbf{x}_s,\mathbf{x}_r)}, \tag{12}$$

where $\dot{\mathbf{s}}$ denotes the synthetic particle-velocity seismograms (obtained by temporal differentiation of predicted synthetic displacement seismograms), and $N(\mathbf{x}_s, \mathbf{x}_r)$ is a normalization factor defined as

$$N(\mathbf{x}_s, \mathbf{x}_r) = \int_0^T w(\mathbf{x}_s, \mathbf{x}_r, t) \left|\dot{\mathbf{s}}(\mathbf{x}_s, \mathbf{x}_r, t)\right|^2 \mathrm{d}t, \tag{13}$$

which represents the energy of the windowed phase in the synthetic particle-velocity seismogram. The travel-time adjoint field $f^\dagger$ is generated by time-reversing the predicted particle velocity at receiver x_r and thus has temporal dependence $T - t$.

Following the finite-frequency theory of [57], perturbations in the total travel-time misfit $\delta\chi$ are linearly related to the relative perturbations in density ($\delta \ln \rho$), S-wave velocity ($\delta \ln \beta$), and P-wave velocity ($\delta \ln \alpha$):

$$\delta\chi = \int_V \left[K_\rho(\mathbf{x})\delta \ln \rho(\mathbf{x}) + K_\beta(\mathbf{x})\delta \ln \beta(\mathbf{x}) + K_\alpha(\mathbf{x})\delta \ln \alpha(\mathbf{x})\right] d^3\mathbf{x}, \tag{14}$$

where K_ρ, K_β, and K_α are the travel-time isotropic Fréchet (sensitivity) kernels for density, S-wave velocity, and P-wave velocity, respectively, and can be computed using the adjoint-state method.

3 Scholte-wave adjoint tomography

Low-frequency (sub-1 Hz) Scholte waves are sensitive to large-scale velocity heterogeneities, such as salt bodies, as demonstrated by ambient wavefield energy recorded on OBN arrays in the Gulf of Mexico [21]. Building on the principles of travel-time adjoint tomography described above, we simulate sub-1.0 Hz Scholte waves recorded by ocean-bottom sensors to evaluate the feasibility of constructing long-wavelength offshore elastic velocity models that incorporate salt structures.

Table 1: 2D synthetic True model parameters.

Model space	V_P (km/s)	V_S (km/s)	ρ (kg/m^3)	Velocity gradients	
				V_P (km/s per km)	V_S (km/s per km)
Background	2.0	0.8	2250	0.40	0.21
Salt	4.5	2.5	2100	—	—

To investigate the influence of individual surface-wave modes and different wavefield components during travel-time tomography, we develop a set of 2-D offshore elastic test models that are presented in Figure 1. The true model (Figure 1, top row) consists of a realistic salt body beneath a flat seafloor located at 0.80 km depth, underlain by 1-D $V_P(z)$ and $V_S(z)$ profiles. Directly below the seafloor, we model a 0.20 km-thick low-velocity layer with $V_S = 0.45$ km/s, beneath which elastic parameters for the background model vary according to the values shown in Table 1. The V_P, V_S, and ρ model components are specified

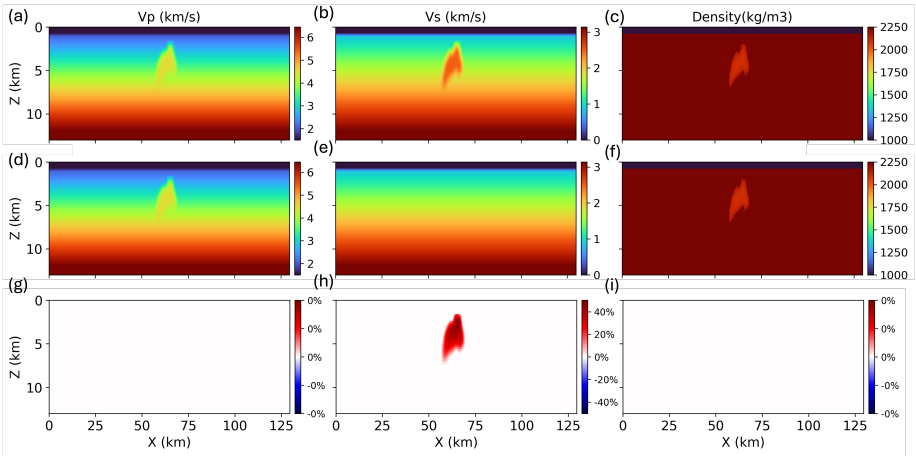

Fig. 1: Synthetic elastic models used for the Scholte-wave adjoint tomography test. The top, middle and bottom rows respectively present the true model and initial model used for tomography, as well as the percentage perturbation between true and initial models. The left, middle, and right columns show the V_P, V_S and ρ model parameters.

just below the low V_S layer and velocities increase with depth as per the aforementioned gradients. The background ρ is kept constant for the entire model. The background velocities are held constant once reaching typical crustal values (approximately $V_P = 6.8$ km/s and $V_S = 3.2$ km/s). These V_P and V_S values and gradients are chosen to be representative of marine clastic sediments found in parts of the Gulf of Mexico [23, 30], although actual gradients can vary significantly due to the effects of local geological processes.

The top of the salt body is located at approximately 1.4 km below the seafloor, extending to a depth of 6.8 km from seafloor, with variable horizontal thicknesses at different depths (see Figure 1). The depth range and varying thickness of the salt body facilitate assessment of the spatial resolution associated with different Scholte-wave wavelengths at varying frequencies. Table 1 also lists the elastic properties of the salt. The overlying homogeneous acoustic water layer is assigned a fluid velocity of $V_f = 1.5$ km/s and a fluid density of $\rho_f = 1000$ kg/m^3. To reduce scattering from sharp interfaces, the model is smoothed around the salt edges using a 2-D convolutional Gaussian filter with standard deviations of two grid points in the horizontal and vertical directions.

The computational mesh extends to 13.0 km in depth and 129.0 km laterally, with a grid spacing of 0.4 km laterally by 0.2 km vertically. The source-time function is a 0.25 Hz central frequency Ricker wavelet designed to capture the spectral content of ambient energy in the secondary microseism band [35, 24, 3] that is commonly observed in long-duration, sparse ocean-bottom seismic recordings at reservoir exploration scales [52, 12, 21, 20].

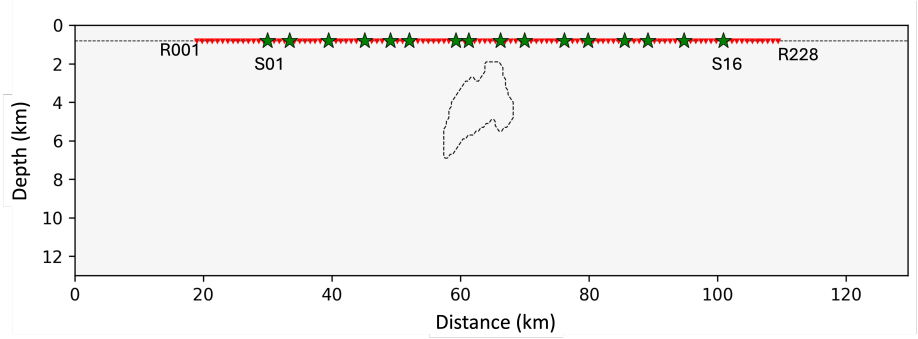

Fig. 2: Sketch of the survey geometry where the red triangles represent ocean-bottom sensors (R001-R228) and blue stars denote source locations (S01-S16). The dotted polygon demarcates the salt boundary.

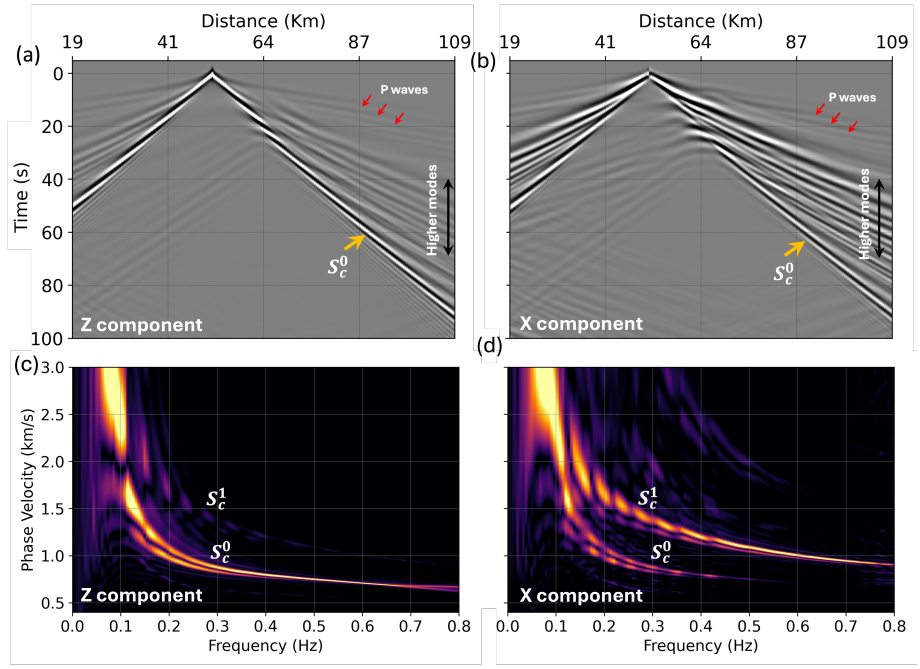

Fig. 3: Data simulated for source S06 recorded at the OBN array. (a) Vertical (Z)- and (b) Horizontal (X)-component shot gather. (c) and (d) Dispersion panels corresponding to (a) and (b), respectively. S_c^0 and S_c^1 denote the fundamental and first-order Scholte modes.

Table 2: Different starting models used in Scholte-wave sensitivity analysis. Here, "True" denotes the true model parameters as described in the text and Table 1 and "Background" is the same model with the salt body removed.

Starting Models	V_P	V_S	ρ
Model A	Background	Background	Background
Model B	$0.9\times$ Background	Background	Background
Model C	True	Background	True

Figure 2 shows the survey geometry. A total of 228 OBNs are deployed 10 m below a flat seafloor at 0.4 km spacing. The array extends from 19.0 km to 109.8 km, forming a receiver line with a maximum offset of 90.8 km. We simulated 16 shots, implemented as vertical point force sources just below the seafloor, with an inter-shot spacing ranging from approximately 2.0 km to 7.0 km. These sources can also be interpreted as virtual sources for constructing empirical Green's functions of surface waves. Note that while the synthetic OBN EGFs used here provide an idealized representation of the true Green's functions—achievable only under perfectly isotropic and stationary ambient source conditions—real-world ambient OBN cross-correlations often deviate from this ideal representation. In practice, uneven or correlated ambient source distributions can introduce intermodal cross-terms and phase mismatches between the retrieved OBN EGFs and the true physical response, as shown in [43]. Nonetheless, with appropriate preprocessing of the real ambient data and physically consistent modeling of the OBN cross-correlations, as described in [44], these effects can be effectively mitigated, thereby preserving the reliability of tomographic updates.

Forward and adjoint wave propagation, along with misfit-kernel calculations, are carried out using the coupled acoustic–elastic capability of `SPECFEM2D`, an open-source spectral-element code [27]. Because perfectly matched layers (PMLs) are currently not available in `SPECFEM2D` for adjoint simulations, the computational domain was extended beyond the source–receiver line to suppress boundary reflections. The mesh spacing is sufficient to simulate surface waves up to 1.0 Hz given the velocity distributions. In `SPECFEM2D`, this maximum resolvable frequency is determined by the spectral-element mesh spacing, ensuring that the shortest wavelengths are sampled by a sufficient number of Gauss–Lobatto–Legendre (GLL) points to accurately represent the wavefield without significant numerical dispersion, while also satisfying the CFL stability condition for time stepping [28]. The free-surface boundary condition is enforced at the top surface, while the remaining boundaries are treated with absorbing layers (Stacey condition).

Particle displacements in the vertical (Z) and horizontal (X) directions for the true model and source S06 are shown in Figure 3a-b, with the corresponding dispersion spectra presented in Figure 3c-d. The shot gathers are dominated by Scholte-wave energy propagating at low velocities, while weaker diving P-wave arrivals are visible at earlier times and moving out with higher velocities. The

fundamental S_c^0 and first-order S_c^1 Scholte modes are clearly identified in the dispersion spectra. In the Z component, the fundamental mode dominates both the shot gather and its dispersion spectrum, whereas S_c^1 exhibits energy comparable to the fundamental mode in the X component. This behavior is consistent with previous observations from four-component ocean-bottom seismometer (OBS) recordings using towed airgun sources [e.g., 46, 15, 60, 61, 49, 21], which have revealed an uneven distribution or partitioning of dispersive energy across the different modal components of the Scholte wavefield. In particular, the X component tends to exhibit more energy from higher-order Scholte modes, while the Z component is typically dominated by fundamental Scholte mode energy.

3.1 Multi-modal surface-wave tomographic sensitivity kernels

Surface-wave propagation in layered media is inherently dispersive and multimodal. Although dispersion characteristics are primarily governed by the V_S profile, V_P influences phase velocities indirectly through its control on the bulk modulus and the resulting Poisson's ratio, which together affect compressibility, compression-shear wavemode coupling (i.e., P–SV and P-SH), and particle-motion characteristics [e.g., 1, 8, 25, 9]. In particular, Scholte waves represent the coupled P–SV solution that propagates along the fluid–solid interface, where both compressional and shear effects contribute to the overall wavefield. Variations in V_P can therefore modify the effective elastic stiffness of the medium and subtly alter dispersion behavior, especially across such interfaces. Consequently, the choice of starting models becomes important in Scholte-wave tomography, as it governs how sensitivity is distributed among different physical parameters and affects their coupling during tomographic inversion.

To examine the sensitivity of Scholte-wave modes to different physical parameters during a single tomography iteration, we employ three distinct starting models derived from the true model, as summarized in Table 2. Model A uses the background properties of the true model for V_P, V_S, and ρ, and thus does not contain the salt body. Model B is similar to Model A but with V_P uniformly reduced to $0.9\times$ the background value, allowing us to assess the effect of a uniformly slower V_P structure. Model C uses the true model parameters for V_P and ρ while retaining the background V_S, enabling us to isolate the impact of shear-velocity variations on the tomographic inversion behavior.

The four rows of Figure 4 compare synthetic, full frequency Scholte-wave waveforms for source S01 across four offset ranges using the true and three approximate starting models presented in Table 2. The black traces represent the true model response, while the red, green, and blue traces correspond to Models A, B, and C, respectively. Each offset group includes three representative stations (left column), along with zoomed-in segments of the Scholte wavetrains highlighted by dotted boxes (right column).

Overall, Models A and C exhibit very similar phase velocities and waveform characteristics, with the red traces (Model C) showing slightly delayed arrivals relative to the blue traces (Model A). This small phase shift indicates that

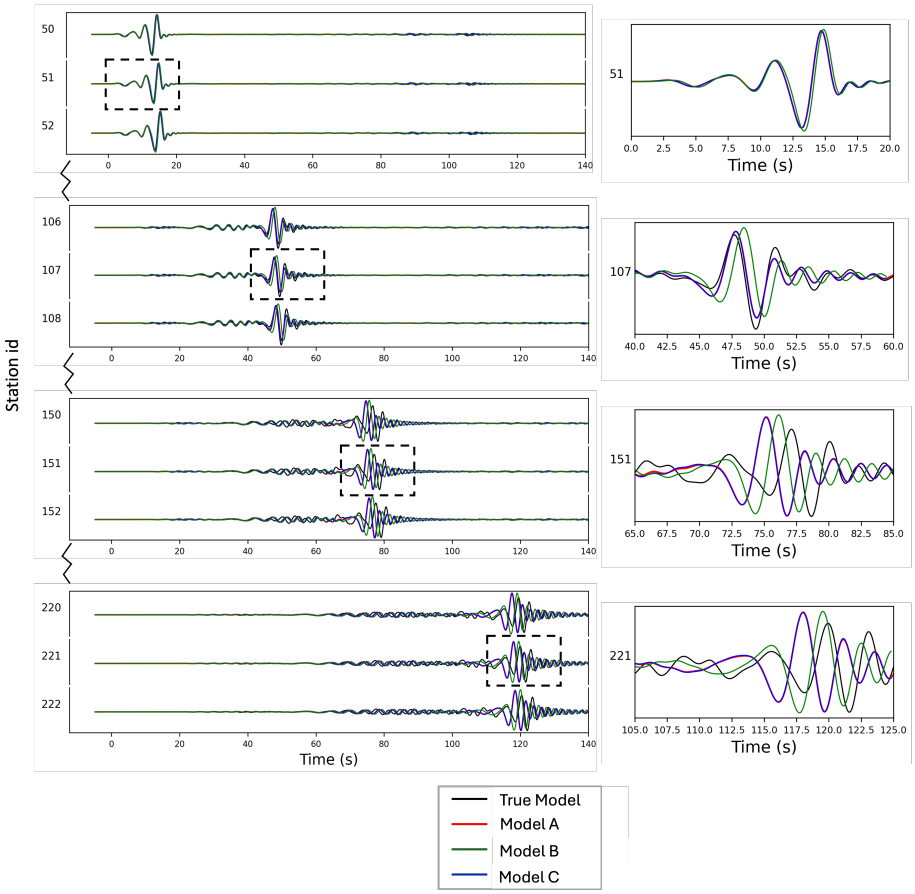

Fig. 4: Left column: Synthetic, full frequency band waveform comparisons of Scholte-wave trains for source S01 at four offset ranges (each row represents one offset) using different starting models described in Table 2, along with the true model. Right column: Zoomed-in traces corresponding to the dotted boxes marked in the left column panels.

introducing the true V_P and ρ distributions in Model C while retaining the background V_S produces only a minor influence on Scholte-wave travel times across the full frequency band. These results suggest that the phase velocity of Scholte waves at these low frequencies is largely insensitive to moderate short-wavelength variations in V_P and ρ (such as the salt body), as the V_S structure dominates the phase-velocity response.

This behavior can also be understood in terms of the dominant wavelengths across the observed frequency range (∼0.1–0.5 Hz). The fundamental Scholte mode has wavelengths of approximately 8–9 km at 0.1 Hz and about 2 km at 0.4 Hz (see Figure 10). Given that the salt body has a vertical extent of roughly 5 km and a lateral extent of 5–10 km within the approximately 90 km modeling domain, the higher-frequency Scholte modes (0.35–0.50 Hz) primarily sample shallower depths and are therefore only moderately influenced by the salt. At lower frequencies, the longer wavelengths more fully overlap with the salt dimensions and the background V_P structure, producing a slightly more noticeable phase delay (not shown here).

By contrast, Model B (green traces) exhibits systematically slower Scholte-wave propagation across all offsets, including the higher-frequency band, unlike Model A. The uniform 10% reduction in V_P decreases the effective stiffness of the medium, resulting in lower phase velocities even though the V_S structure remains unchanged. This demonstrates that large-scale V_P perturbations, such as those applied uniformly across the background model, can indirectly affect Scholte-wave propagation across the entire observed frequency band by modifying Poisson's ratio and the elastic coupling at the water–sediment interface. The influence of interface compliance is wavelength-dependent: shorter-wavelength modes are primarily sensitive to local, near-surface stiffness, whereas longer-wavelength Scholte modes—dominant at intermediate and far offsets—sample deeper velocity contrasts and the integrated compliance of the boundary. Consequently, phase delays are more pronounced for long-wavelength modes, highlighting the importance of V_P structure in controlling effective stiffness and wave propagation even when V_S remains fixed.

To further analyze parameter sensitivities, we computed the preconditioned travel-time sensitivity (Fréchet) kernels for V_P (K_α), V_S (K_β), and ρ (K_ρ) after the first travel-time tomography iteration. Event kernels were stacked over sources and preconditioned using a pseudo-Hessian derived from the diagonal Hessian approximation [32, 67, 38] given by

$$P(\mathbf{x}) = \sum_{s=1}^{N_s} \int_0^T \ddot{\mathbf{s}}_s(\mathbf{x}, t) \cdot \ddot{\mathbf{s}}_s^\dagger(\mathbf{x}, T-t) \mathrm{d}t, \tag{15}$$

where $\ddot{\mathbf{s}}_s$ and $\ddot{\mathbf{s}}_s^\dagger$ denote the forward and adjoint acceleration fields for the s-th source, respectively; N_s is the number of sources; and $t \in [0, T]$ with T being the total analysis or propagation time. The preconditioned misfit kernels were subsequently smoothed with a 2-D convolutional Gaussian filter (horizontal and vertical widths of 1.6 km and 0.8 km, respectively). Preconditioning redistributes sensitivity away from the surface and stabilizes depth scaling. Fig-

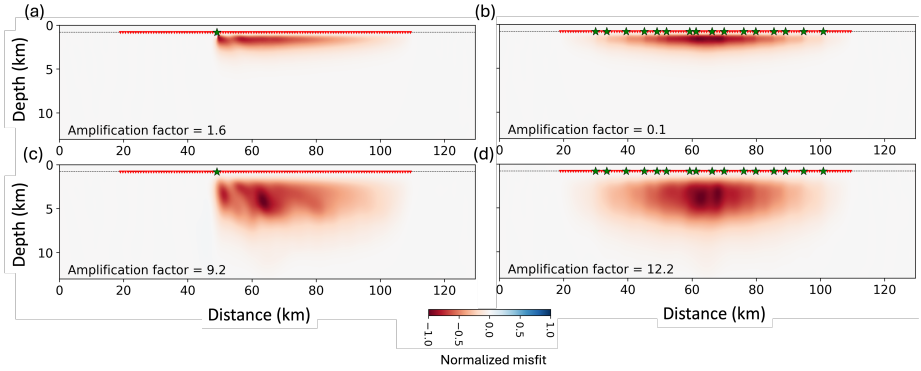

Fig. 5: Model C (see Table 2) V_S misfit kernels after the first travel-time tomography iteration with waveforms low-pass filtered to 0.2 Hz. Kernels for (a) S06 and (b) all sources prior to smoothing and preconditioning. (c) and (d) smoothed and preconditioned kernels associated with those shown in (a) and (b), respectively. Misfits are calculated between the initial and true models. The amplification factor indicated below each plot denotes the scaling applied relative to the colorbar for visualization.

ure 5 illustrates the effect of preconditioning on travel-time sensitivity kernels. The left column shows kernels for a single event, while the right column displays kernels combined over all events. The top row presents unpreconditioned kernels, which are strongly concentrated near the surface, reinforcing the shallow sensitivity of Scholte waves due to receivers located at the seafloor, as the Scholte waves sensitivity to V_S tend to be concentrated near stations. As a result, model updates are disproportionately large near the seafloor. The bottom row shows preconditioned, smoothed kernels, where values are appropriately scaled, producing a more balanced sensitivity distribution at greater depths.

Figure 6 shows the misfit kernels for V_P, V_S and ρ after the first travel-time tomography iteration for Model A, with the fundamental mode displayed in the left panels and higher-order modes in the right panels. The V_S kernels exhibit substantially higher amplitudes compared to those of V_P and ρ, with almost no energy appearing in the V_P kernels. This indicates that tomography using fundamental or higher-order mode data will result in negligible changes to the V_P model and underscores the dominant sensitivity of Scholte-wave energy to V_S perturbations.

Figure 7 shows the fundamental-mode misfit kernels for Model B where V_P is uniformly reduced to 0.9× the background value; higher modes show qualitatively similar behavior and thus are not shown. As in Model A, the V_P kernels display negligible energy, indicating minimal sensitivity of the travel-time misfit to V_P variations. These observations suggest that neither the fundamental nor higher Scholte modes significantly influence the V_P update during tomographic inversion. In contrast, the V_S kernels retain strong and spatially coherent sensi-

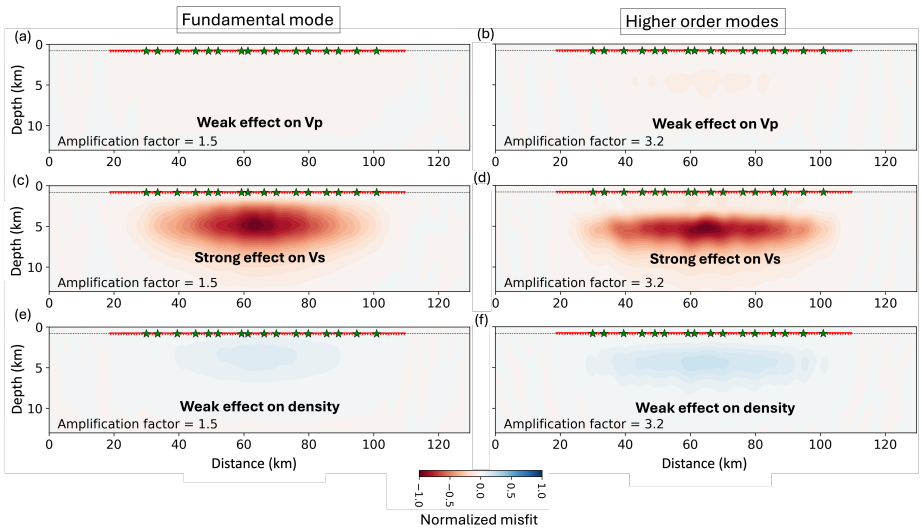

Fig. 6: Stacked, preconditioned misfit kernels after the first travel-time tomography iteration for Model A (see Table 2) using Z-component waveforms low-pass filtered to 0.1 Hz. The left and right columns show Z- and X-component data, while the top, middle and bottom rows show V_P, V_S, and ρ kernels, respectively.

tivity, while the ρ kernels show low-amplitude but spatially correlated patterns, which implies only a secondary and weak coupling with the shear-velocity model structure.

Overall, the waveform and kernel analyses demonstrate that Scholte-wave tomography is overwhelmingly sensitive to V_S variations, whereas the effects of V_P and ρ are weak or indirect. Large perturbations in V_P can influence propagation through elastic coupling, potentially introducing measurable phase delays that may affect cycle skipping and inversion convergence, and influence parameter crosstalk in multi-parameter Scholte-wave tomography. However, tomographic inversion gradients remain dominated by V_S, meaning that surface-wave-based tomographic inversions primarily update the V_S field, with limited recovery of V_P and ρ. This highlights that having an accurate background V_P model—particularly in regions without significant secondary V_P anomalies—provides a robust starting point for Scholte-wave tomographic inversions.

3.2 Shear-velocity sensitivity and mode-dependent tomography

The technical objective of this investigation is to recover the long-wavelength elastic structure, particularly V_S, in high-contrast bodies such as salt using long-duration ambient ocean-bottom recordings that capture surface waves in the sub-1.0 Hz frequency band. As shown in the misfit-kernel analyses (Figures 6

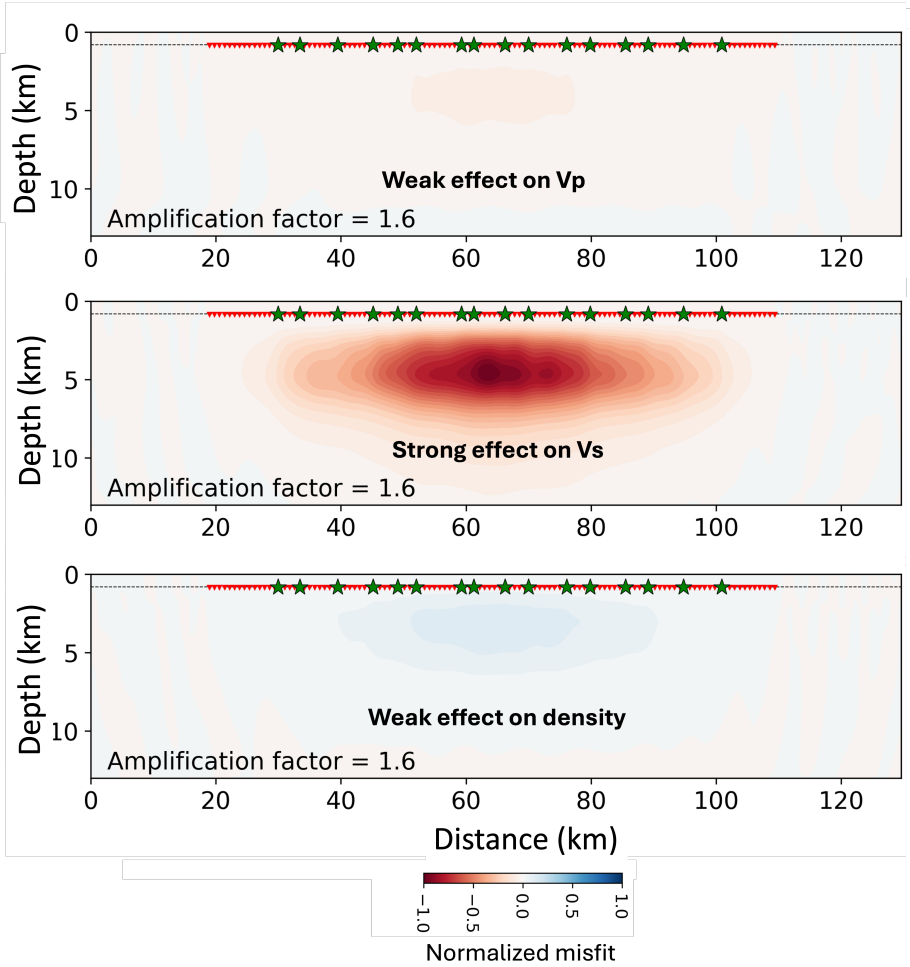

Fig. 7: Stacked preconditioned misfit kernels using fundamental mode after the first travel-time tomography iteration for Model B (see Table 2) using Z-component waveforms low-pass filtered to 0.1 Hz. The top, middle and bottom panels present the V_P, V_S, and ρ kernels, respectively.

and 7), Scholte-wave tomography is highly sensitive to V_S variations, while sensitivity to V_P and ρ is weak or indirect. Although large V_P deviations can affect wave propagation and introduce measurable phase delays, adjoint-state tomographic inversion gradients remain dominated by V_S. Consequently, starting with an accurate V_P and ρ model ensures that surface-wave-based updates primarily target the shear-velocity field, minimizing crosstalk from erroneous V_P or ρ models.

In this set of tests, we assume that active-source acoustic FWI has already exploited recorded body waves to produce a high-resolution V_P model. Accordingly, our starting model (Figure 1, middle row) retains the V_P distribution but adopts a V_S model defined by the background velocities (i.e., excluding the salt), resulting in a V_S anomaly ranging from approximately 10% (∼0.3 km/s) near the base of the salt to about 50% (∼1.2 km/s) near the top (Figure 1, bottom row). Background velocities can be estimated using appropriate empirical V_P–V_S relations for the study area. The ρ distribution is also inherited from the V_P model, ensuring consistency in the representation of the salt structure, with the ρ contrast between salt and background relatively small (150 kg/m^3 or 6.7%) compared to the V_S contrast. This set of starting model parameters is referred to as Model C in Table 2.

Figure 8 presents synthetic source S01 waveforms over the full frequency band for both Model C and the true model at receivers R95–R125. The comparisons reveal phase delays of Scholte-wave trains in the initial model relative to the true model starting at R106 that are caused by the high-V_S salt structure present beneath that receiver location. These delays increase with offset. In Figure 8a, at larger offsets, the fundamental Scholte phase (shaded in light orange) from the initial model appears to arrive slightly earlier around R120, although it still lags by less than half a cycle compared to the true model arrivals. This behavior reflects the dispersive nature of surface waves and illustrates the potential for cycle skipping even when phase differences are small.

The effect is more pronounced in the X component, where the fundamental Scholte phase from the initial model seems faster for receivers (around R107) at offsets closer to S01. In contrast, higher-order Scholte wave trains (shaded in light blue) have comparable energy to the fundamental on the X component but much weaker energy relative to the fundamental on the Z component. Importantly, they exhibit much smaller phase delays, do not arrive earlier, and remain in phase lag by less than half a cycle relative to the true-model waveforms, even at large offsets, thus avoiding the cycle-skipping problem.

Surface-wave tomographic inversions typically rely on the fundamental mode, as it is the most energetic and easiest to identify. However, as seen in the synthetic waveforms above the fundamental mode is susceptible to dispersive effects and cycle skipping at larger offsets, particularly in the presence of strong velocity contrasts such as salt bodies, whereas higher-order modes remain largely in phase. To address these challenges, tomographic inversion seeks to exploit all observable modes, and hierarchical frequency-stepping scheme—progressing from lower to higher frequencies—to mitigate dispersion-related artifacts, following strategies analogous to those used in active-source FWI [6].

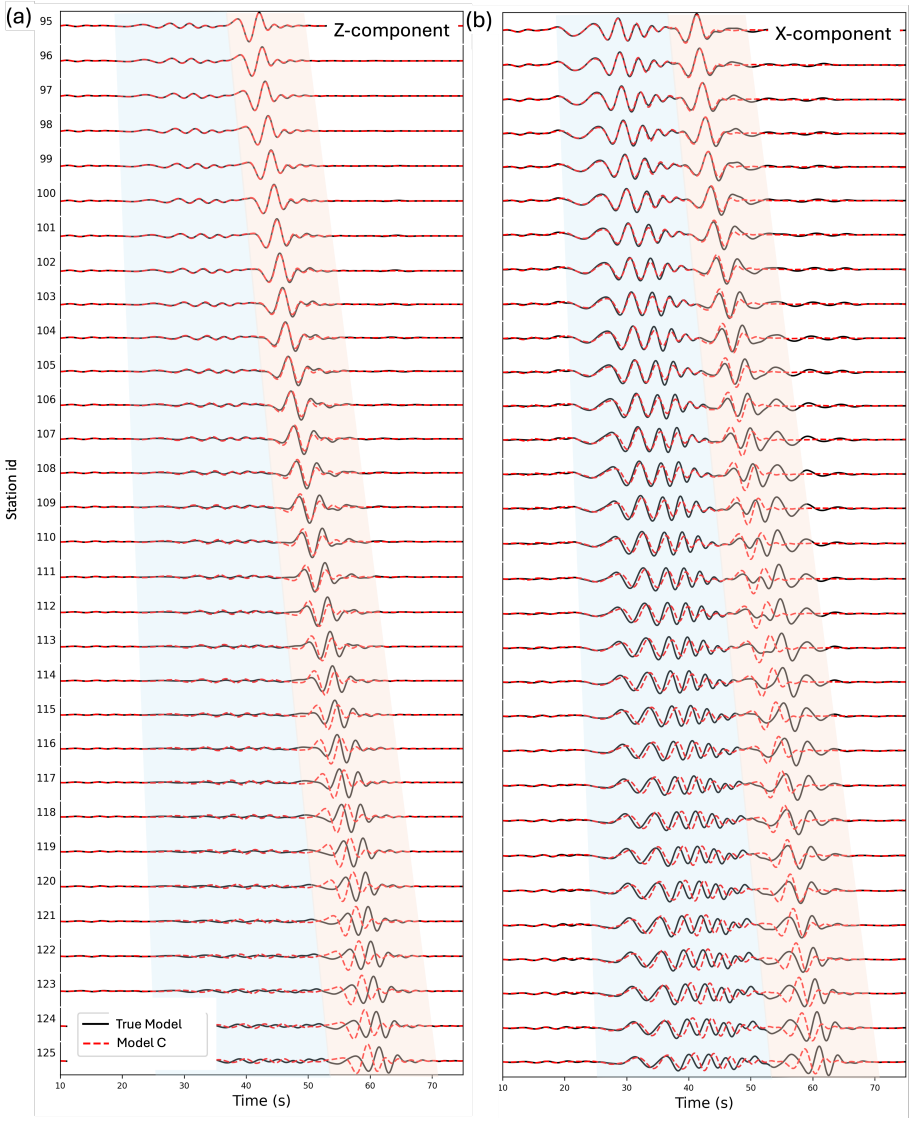

Fig. 8: Synthetic S01 source waveform comparison for Scholte wave trains. (a) Z- and (b) X-component data. The solid black and dotted red curves represent synthetic waveforms from the true model and Model C (used as starting model for tomographic inversion), respectively. The orange and blue shaded regions indicate the time windows (i.e., w function in equation 11) for the fundamental- and the higher-order Scholte phase arrivals, respectively. Each waveform is normalized with respect to its corresponding observed trace.

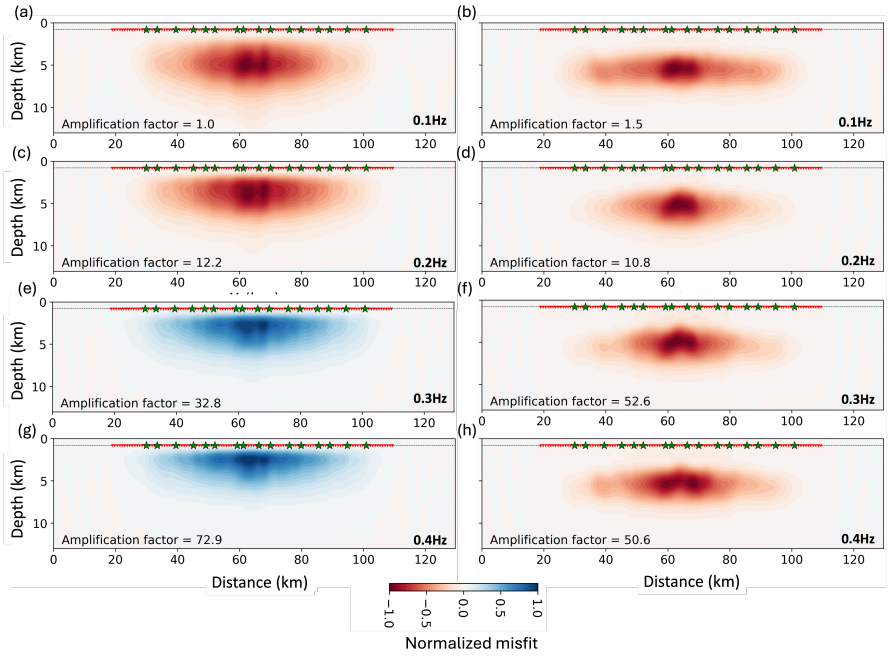

Fig. 9: Stacked preconditioned V_S misfit kernels after the first travel-time tomography iteration using Z-component waveforms from Model C (see Table 1). The left column shows the fundamental Scholte mode, and the right column shows the higher-order Scholte modes. Each row corresponds to a different low-pass frequency band: (a-b) 0.1 Hz, (c-d) 0.2 Hz, (e-f) 0.3 Hz, and (g-h) 0.4 Hz.

To systematically investigate the contributions of individual Scholte-wave modes at different frequencies during tomographic inversion, we analyze synthetic vertical and horizontal seismograms alongside their corresponding V_S sensitivity kernels (K_β). Prior to kernel calculation, waveforms were low-pass filtered at four cutoff frequencies—(a) 0.1 Hz, (b) 0.2 Hz, (c) 0.3 Hz, and (d) 0.4 Hz—and separated into fundamental and higher-order modes by manual muting before the misfit-kernel calculation. Individual event misfit kernels were computed in the first inversion iteration at these frequencies, after which the event kernels were stacked, preconditioned, and smoothed as described earlier. While the relative amplitudes of the misfit kernels are not preserved, an amplification factor is included at the bottom of the plots where appropriate, facilitating comparison of relative amplitudes across panels with respect to the unit-normalized misfit colorbar.

Figure 9 shows the 2-D V_S misfit kernels for the fundamental (left column) and higher-order Scholte modes (right column) across different frequencies, while Figure 10 presents the corresponding normalized 1-D depth sensitivities obtained by laterally summing the 2-D kernels. Both figures highlight sev-

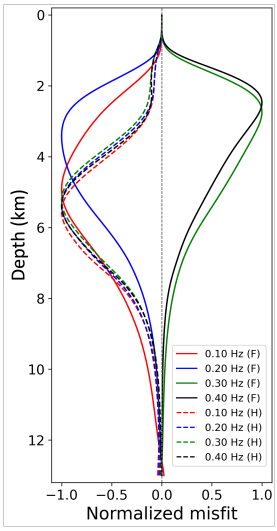

Fig. 10: 1-D V_S sensitivity kernel obtained by summing and normalizing the kernels along the horizontal distance axis in Figure 9. Solid curves represent the fundamental modes (F), while dotted curves indicate higher-order modes (H). The fundamental-mode amplitudes at 0.3 Hz and 0.4 Hz are reversed relative to the others due to cycle skipping.

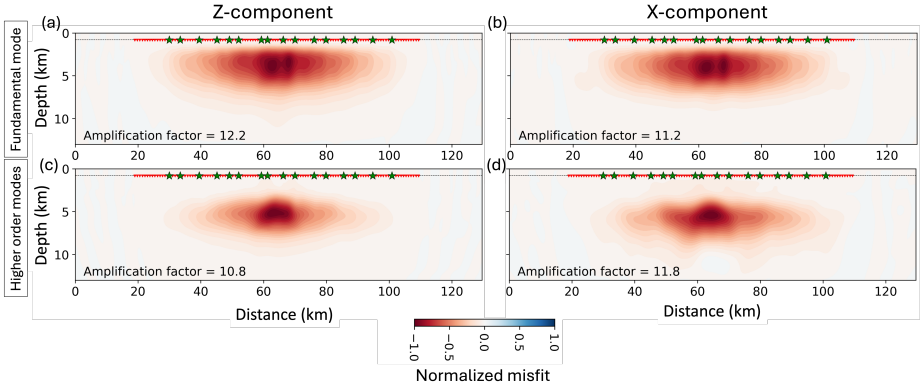

Fig. 11: Stacked, preconditioned V_S misfit kernels after the first travel-time tomography iteration using Model C (see Table 1), with waveforms low-pass filtered to 0.2 Hz. Left column: Z-component data; right column: X-component data. Top row: fundamental mode; bottom row: higher-order modes.

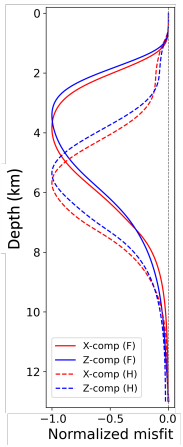

Fig. 12: 1-D V_S sensitivity kernel obtained by summing the kernels along the horizontal distance axis in Figure 11. Solid lines represent the fundamental modes (F), while dotted lines indicate higher modes (H). The blue and red curves shows the sensitivity of the Z and X components, respectively.

eral key characteristics. First, lower frequencies penetrate significantly deeper than higher frequencies (e.g., the 0.1 Hz fundamental mode in Figure 10 has maximum sensitivity around 6.0 km depth). In addition, the sensitivity systematically shifts toward shallower depths with increasing frequency, reflecting the depth-dependent nature of model updates. However, the magnitudes of these contributions vary with frequency (see amplification factors for comparison). Second, higher-order modes within a given frequency band penetrate deeper than the fundamental mode and thus contribute a higher update weight at greater depths (e.g., solid versus dashed green curves at 0.1 Hz in Figure 9). Third, the fundamental mode has stronger frequency dependence as exhibited by more pronounced shifts in depth sensitivity, whereas higher-order modes vary more gradually (see Figure 10 where the 1-D kernels clarify these depth-dependent trends). At low frequencies, the fundamental mode (e.g., solid red curve at 0.1 Hz) has broad sensitivity suitable for recovering long-wavelength structures, while higher frequencies (e.g., solid green curve at 0.3 Hz) enhance sensitivity to shallower features. In contrast, higher-order modes maintain sensitivity to deeper regions. In all cases, sensitivity decays rapidly with depth.

An additional observation is the polarity reversal due to cycle skipping in the fundamental-mode kernel at 0.3 Hz and 0.4 Hz (Figure 9e, Figure 9g and the solid green and solid black curves in Figure 10) where amplitudes switch from negative to positive. At the same frequency, higher-order modes continue to correlate with the correct phase and do not experience cycle skipping. In fact, although the combined kernel is negative at 0.2 Hz, traces at large offsets exhibit cycle skipping as well. This highlights the importance of frequency stepping in surface-wave tomographic inversion, analogous to active-source FWI methodol-

ogy. Because of their dispersive character, surface waves are particularly prone to cycle skipping; however, this risk is reduced at lower frequencies, increasing the likelihood of convergence toward the global minimum.

Figure 11 shows the contributions to the V_S misfit kernel from the Z and X particle-displacement components for Scholte modes at 0.2 Hz. The left and right columns correspond to the Z and X components, while the top and bottom rows show the fundamental and higher-order mode sensitivities, respectively. Figure 12 presents the corresponding 1-D depth sensitivities obtained by laterally summing the 2-D kernels. Although the fundamental-mode misfits for both components have similar magnitudes (see amplification factors), the X component exhibits slightly deeper sensitivity than the Z component (Figure 12). Higher-order modes penetrate deeper than the fundamental mode, with the X component again providing slightly deeper coverage than the Z component.

Overall, the combined set of observations emphasizes the importance of exploiting multiple modes and frequencies in surface-wave tomographic inversion, as they provide complementary sensitivities at different depths and enable more robust model updates.

3.3 Multi-modal Scholte-wave tomography

3.3.1 Parameters from Model C as starting model

We now present the inverted V_S model obtained from adjoint tomography using parameters from Model C as the starting model. At each iteration, waveform preprocessing (i.e., filtering, normalization, and window selection for both fundamental and higher-order Scholte modes), misfit calculation, and adjoint-source construction are performed using the `pyflex` [36], `pyadjoint`, and `pyatoa` packages integrated into the `SeisFlows` waveform inversion package [39, 11] that incorporates `SPECFEM2D` as the forward and adjoint wave-propagation solver. Model updates are carried out using the L-BFGS method [31], while a line-search procedure determines the optimal step length (see equation 8) at each iteration. For further details on the adjoint inversion methodology, we refer readers to [59].

The tomographic inversion begins from a background V_S model without salt, i.e Model C (Figure 1). Forward simulations are first performed using this initial model, with Z-component waveforms low-passed at 0.10 Hz to emphasize long-wavelength structures during the early stages of inversion. Both fundamental and higher-order Scholte modes are used to quantify the misfit and compute adjoint sources. The inversion proceeds by progressively incorporating higher-frequency data as the misfit reduction from the current band either saturates or the model updates become negligible. We start with the low-frequency band ($\leq$0.10 Hz), then incrementally add waveforms from 0.20 Hz, 0.30 Hz, 0.40 Hz, and 0.45 Hz bands (see Figure 13). Figure 13a shows the misfit reduction on a linear scale, where reductions appear modest after the tenth iteration but still produce significant model updates. Figure 13b presents the same results on a

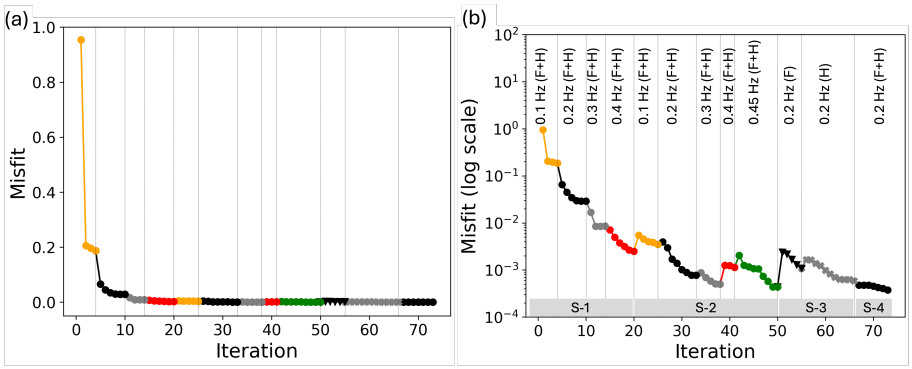

Fig. 13: Cross-correlation travel-time misfit reduction. (a) Linear scale. (b) Logarithmic scale emphasizing small changes in misfit reduction. Misfit segment colors denote low-pass frequency bands: orange (0.10 Hz), black (0.20 Hz), gray (0.30 Hz), red (0.40 Hz), and green (0.45 Hz). Markers indicate the modes used for misfit and adjoint source calculations: solid dots (F+H), inverted triangles (F), and crosses (H). Each region is also annotated with the frequency band and mode(s) used for misfit and adjoint calculations. In (b), the regions labeled S-1 to S-4 represent the four inversion stages.

logarithmic scale where misfit changes are now more clearly visible.

Figure 13b highlights the four stages of inversion (S-1 through S-4) used to obtain the results shown in Figure 14 starting from the models presented in panels a and f.

- S-1 (iterations 0–20): Involves sequential frequency stepping from 0.10 Hz to 0.40 Hz using both fundamental and higher-order modes. Each frequency increment helps the inversion escape local minima, achieve new misfit reductions, and builds the initial salt structure (Figure 14b and 14g).
- S-2 (iterations 20–50): Repeats this multiband strategy from 0.10 Hz to 0.45 Hz to further refine the salt structure. By the end of S-2, the combined misfit across all modes decreases to the order of 10^{-4}. Although the total misfit is substantially reduced, misfits from individual modes remain relatively larger (Figure 14c and 14h).
- S-3 (iterations 51–67): Alternates between mode-specific inversions. Iterations 50–54 use only the 0.20 Hz fundamental mode, followed by iterations 54–67 using only higher-order modes at 0.30 Hz. This strategy further sharpens both large-scale salt background and smaller-scale structural details of the salt body (Figure 14d and 14i).
- S-4 (iterations 68–72): Incorporates additional updates with all Scholte modes at 0.20 Hz; however, the misfit reduction and model updates during

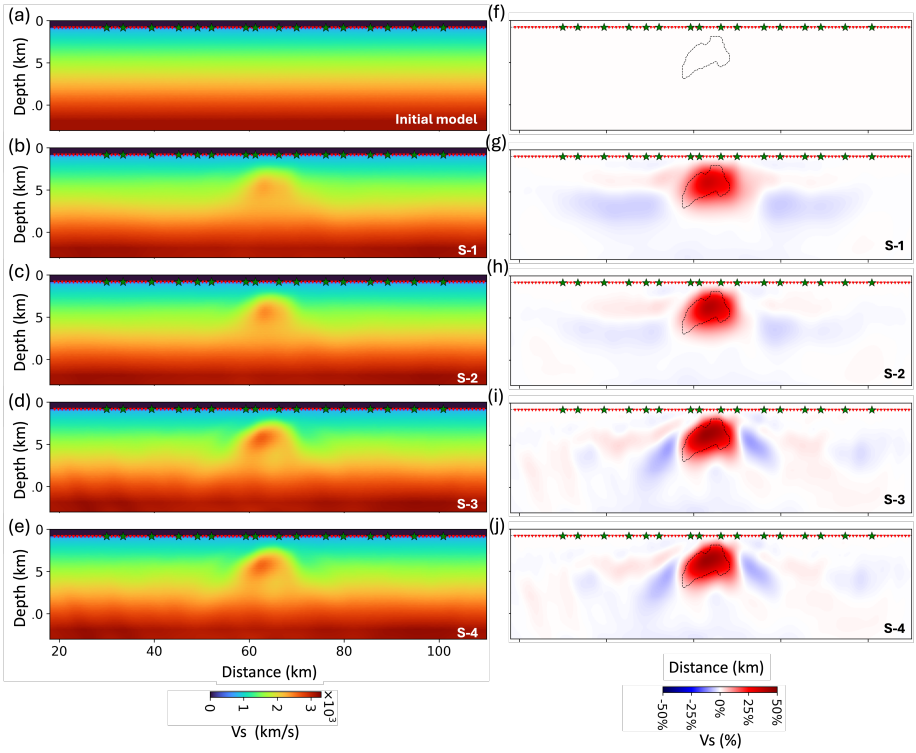

Fig. 14: Left: V_S model recovery during inversion stages from the initial model (Model C) to stages S-1 through S-4 (see Figure 13b). Right: Differences between the recovered and initial models, showing the evolution of V_S updates across stages S1–S4, relative to the percentage perturbation between the true and initial models. The dotted polygon marks the salt boundary.

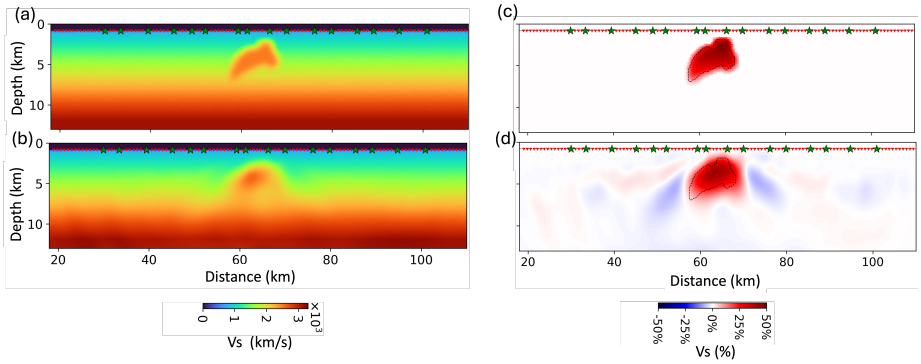

Fig. 15: (a) True and (b) inverted V_S models. (c) Percentage V_S perturbation between the true and initial models (Model C). (d) Percentage perturbation recovery relative to (c) after inversion.

this final stage are minimal (Figure 14), indicating that the inversion has converged (Figure 14e and 14j).

At the S-1 stage, we applied a Gaussian smoothing filter to the stacked and preconditioned gradient kernels with vertical and horizontal window lengths of 1.6 km and 0.8 km, respectively. Between S-2 and S-4, the window sizes were reduced to 0.8 km and 0.4 km to accommodate higher-frequency measurements [54, 38].

Figure 15 compares the true and inverted V_S models. The tomographic inversion successfully recovers the overall long-wavelength geometry of the salt body (Figure 15d). Figure 16 shows the difference between the inverted and true V_S models, along with comparisons of the true, inverted, and initial V_S model along three vertical profiles across the salt body. From Figure 16b–d, it is evident that the model recovery at intermediate depths is robust, with velocities reproduced within approximately 10% of the true values. However, velocities at salt depths greater than ∼6 km are less accurately recovered, and in regions of shallow salt (Profile C; Figure 16d), the inversion remains poorly constrained. The relatively poor recovery in both deeper and shallower regions is likely due to the limited frequency range used: frequencies lower than 0.10 Hz are required to image deeper structures, while frequencies higher than 0.45 Hz would be needed to better constrain the shallow salt velocity field.

3.3.2 Parameters from Model A as starting model

As shown earlier, the influence of salt V_P and ρ on Scholte-wave kinematics is relatively minor across the 0.1–0.5 Hz band, motivating an additional tomographic inversion using Model A (V_P, V_S, and ρ all set to the background with no salt). Starting from Model A, we follow the same staged, multi-modal

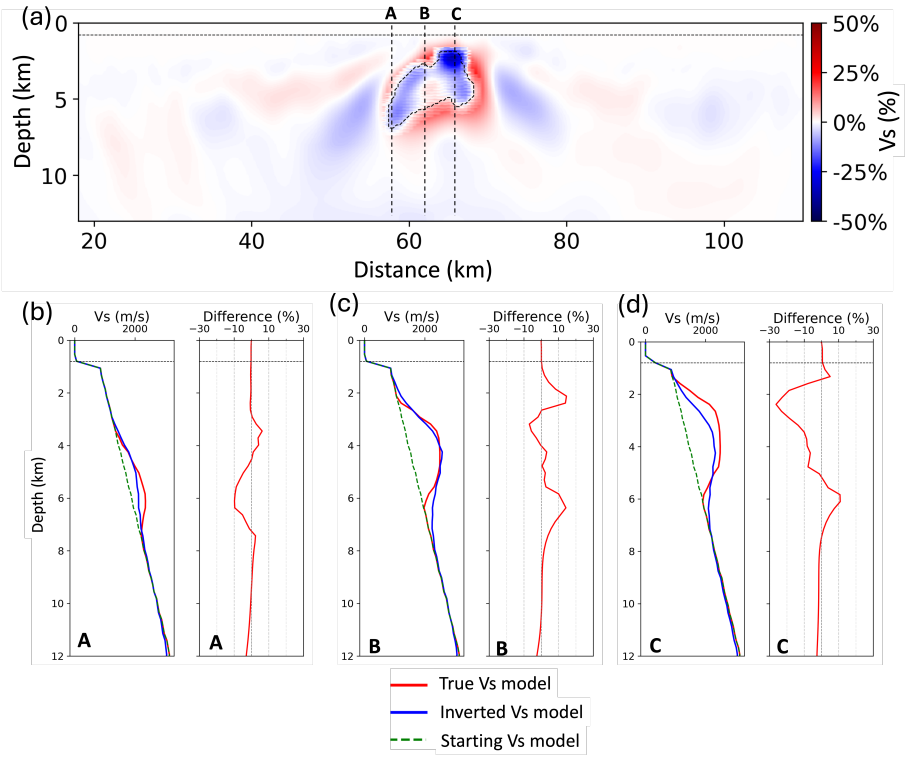

Fig. 16: (a) Percentage difference between the recovered and true model V_S relative to the true model. (b)–(d) show the true, inverted, and initial V_S profiles, together with the percentage differences, along slices A, B, and C, as marked in (a).

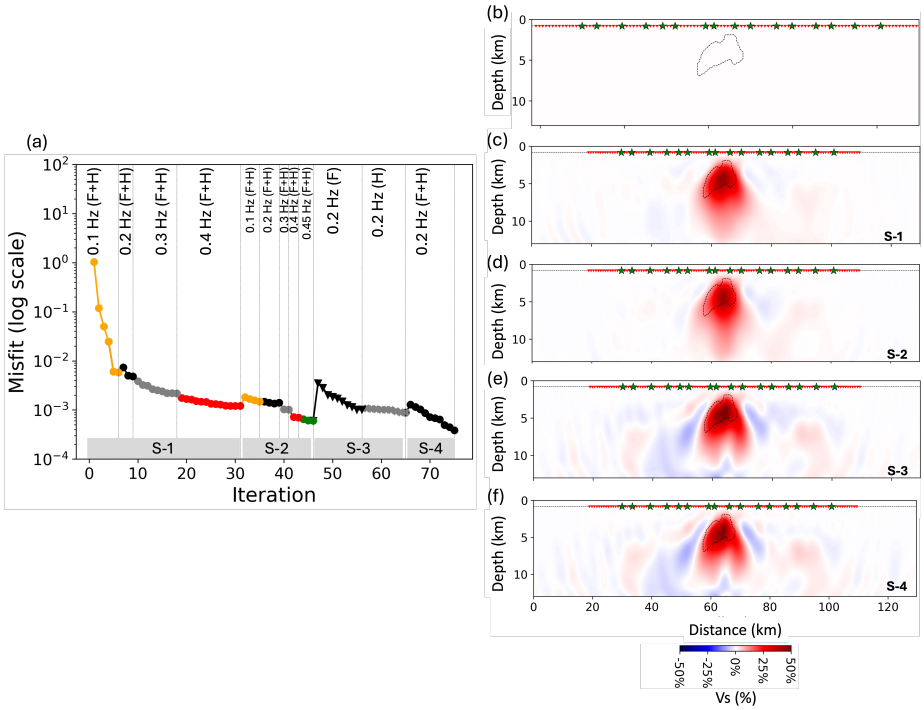

Fig. 17: Left: Log-scale cross-correlation travel-time misfit reduction with parameters from Model A as the starting model. The regions labeled S-1 to S-4 represent the four inversion stages. For color codes and labels explanation, see Figure 13. Right: Differences between the recovered and initial models, showing the evolution of V_S updates across stages S1–S4, relative to the percentage perturbation between the true and initial models. The dotted polygon marks the salt boundary.

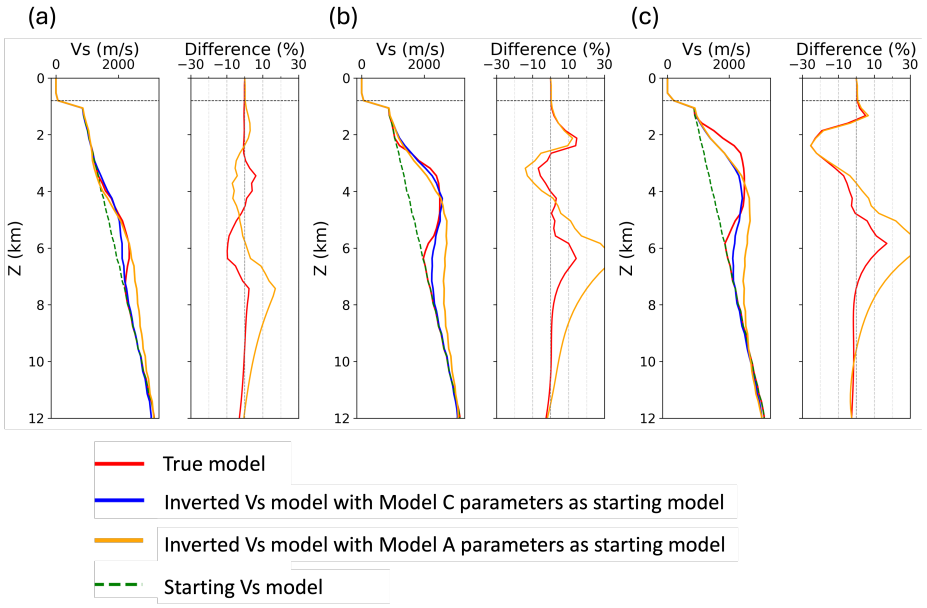

Fig. 18: (a)–(c) show the true, inverted, and initial V_S profiles, together with the percentage differences, along slices A, B, and C, as marked in Figure 16a.

frequency-stepping workflow used for Model C in the previous section (S-1→S-4), producing the log-scale misfit reduction and model-update evolution shown in Figure 17. During this inversion, only V_S was updated, while V_P and ρ remained fixed to their background values.

The recovered model reproduces the overall long-wavelength geometry of the salt body, with the stage-by-stage updates and shape recovery summarized in Figure 17c–f. The inversion yields reasonably accurate velocities at intermediate depths (within 10%; see Figure 18). These results demonstrate that, even when neither V_P nor ρ encode the true salt, the dominant sensitivity of Scholte-wave travel times to V_S enables robust lateral shape recovery and substantial recovery of intermediate-depth shear velocities. However, despite the generally good lateral recovery, the inversion with Model A as the starting model populates anomalously high V_S values beneath portions of the salt while maintaining good lateral constraint (see Figure 17c–f).

This behavior can be understood from the Scholte-wave misfit kernels and sensitivity analyses presented earlier, which confirm that inversion gradients are strongly dominated by V_S, while V_P and ρ influence the results only indirectly through elastic coupling and Poisson's ratio contrasts. When V_P and ρ do not capture the true salt contrasts, the inversion compensates for small phase misfits arising from these inaccuracies by increasing V_S at depth to match the observed travel times (i.e., parameter trade-offs and crosstalk), particularly at

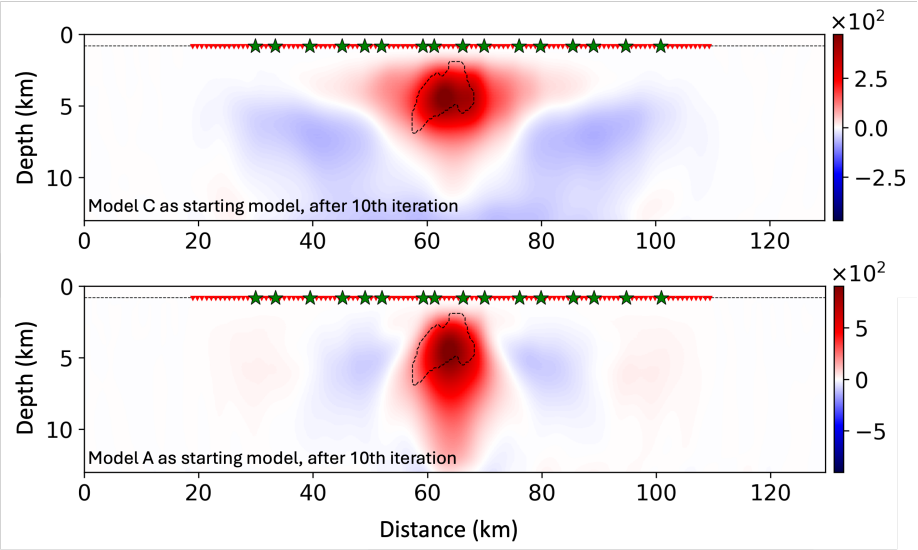

Fig. 19: Inverted V_S models after the 10th iteration using (a) Model C parameters and (b) Model A parameters as starting models.

low frequencies where the longer wavelengths of Scholte waves sample the full extent of the salt. Consistent with this interpretation, the earlier comparison between Model A and C traces (Figure 4) shows that introducing the true V_P and ρ distributions produces only a minor effect on Scholte-wave travel times and phase velocities across the 0.1–0.5 Hz band, although the influence becomes more noticeable at lower frequencies due to enhanced sensitivity to the salt.

The additional low-frequency results after the tenth iteration shown in Figure 19 further illustrate this behavior: with Model A, anomalously high V_S values—relative to the recovered shear velocity of the salt—begin to appear beneath the salt early in stage S-1, when the inversion incorporates 0.10–0.20 Hz data (see Figures 13 and 17a). These artifacts likely originate from low-frequency phase misfits induced by inaccurate V_P and ρ starting model. In contrast, the corresponding Model C results show improved depth focusing and reduced low-frequency misfits due to the presence of the true V_P and ρ distributions.

Nevertheless, the lateral geometry remains well constrained. Compared with the Model C runs (true V_P and ρ, background V_S), the shape and resolution of the recovered salt are somewhat improved when V_P and ρ are correct, indicating that accurate V_P/ρ priors help reduce parameter trade-offs and vertical smearing.

4 Impact of elastic structure on amplitude fidelity

The Introduction section emphasized the importance of elastic modeling and accurate V_S estimation for capturing the true physics of wave propagation. Having established that Scholte-wave travel-time tomography can recover reliable long-wavelength V_S structures, we now examine the implications of these models for amplitude fidelity of forward modeled wavefields. This analysis assesses how accurately the recovered elastic model reproduces the amplitude behavior of full elastic wave propagation compared to when invoking an acoustic approximation.

To this end, we simulate the vertical-component (Z) waveforms from the true model using both elastic and acoustic physics. The simulations employ an Ormsby source wavelet with corner frequencies of [1.8, 3.0, 5.0, 9.0] Hz, representative of the low-frequency end of active-source seismic data, with the source S06 now positioned just below the ocean surface as a pressure source to mimic an active-source ocean-bottom node (OBN) acquisition geometry. Figure 20a shows the modeled Z-component wavefield for the true model, where diving-wave energy is evident and effect of the salt can be seen around 60 km offset where diving waves exhibit faster move out.

Figure 20b presents trace panels extracted from three locations marked A, B, and C in Figure 20a. Each panel includes three traces: (1) the true model simulated with full elastic physics (solid black curve); (2) the true model simulated using the acoustic approximation (dashed black curve); and (3) using the inverted long-wavelength V_S model from starting Model C and elastic physics (solid red curve).

From Figure 20b, we observe that the direct P-wave arrivals exhibit comparable amplitudes across all three cases. However, significant amplitude discrepancies arise in the arrivals associated with P–S mode conversions when comparing the elastic and acoustic simulations of the true model. These differences highlight the inability of the acoustic approximation to reproduce the amplitude variations governed by the elastic shear modulus and Poisson's ratio contrasts. In contrast, when the inverted long-wavelength V_S model is used with elastic physics, the resulting amplitudes show strong agreement with the true elastic response, particularly in the converted phases.

These results demonstrate that even a smooth, long-wavelength V_S model recovered from Scholte-wave tomography can significantly improve the amplitude accuracy of elastic simulations relative to those generated through acoustic modeling. The consistency between the true and inverted elastic responses confirms that accurate representation of the background shear-wave velocity structure is essential for reproducing realistic mode conversions and amplitude variations. This finding underscores the broader implication that elastic forward modeling, when guided by an appropriately constrained V_S model, can yield amplitude-consistent synthetic data suitable for subsequent high-frequency E-FWI, or joint inversion workflows that rely on amplitude information.

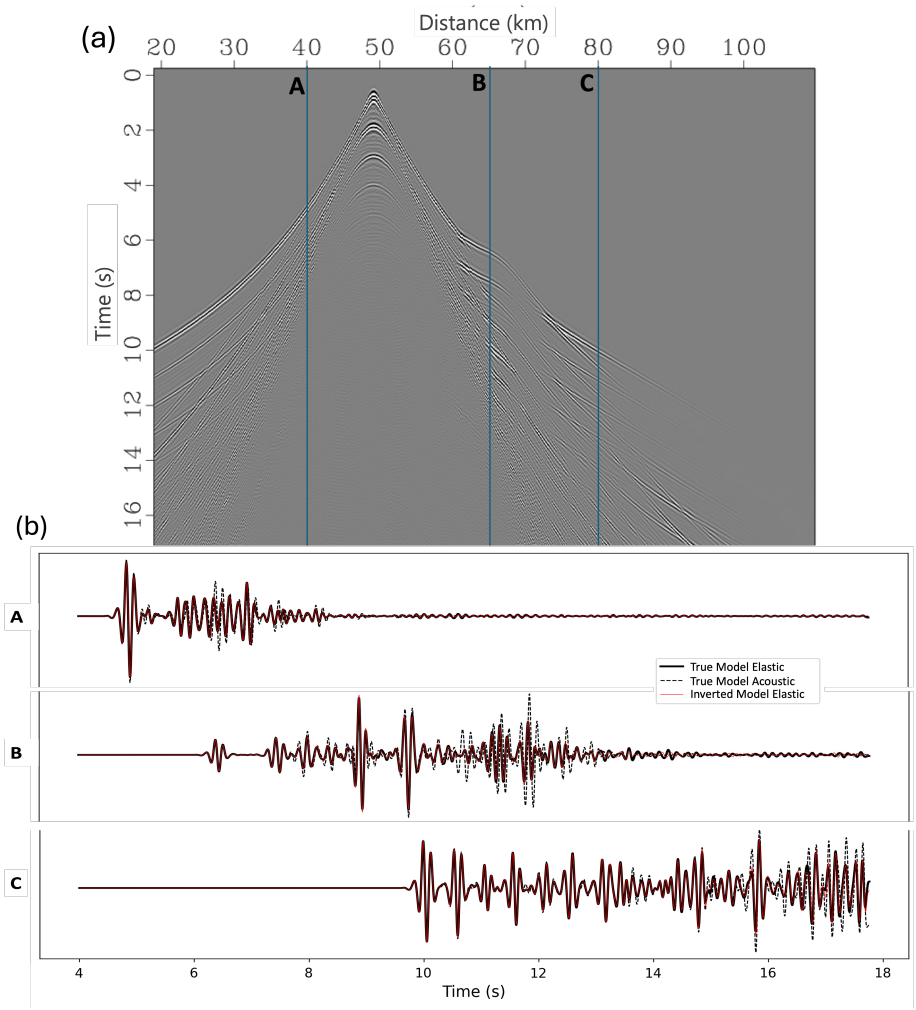

Fig. 20: (a) Z-component shot gather generated using the true model (Figure 1, top row) and an Ormsby wavelet with corner frequencies [1.8, 3.0, 5.0, 9.0] Hz, for a pressure source S06 positioned just below the ocean surface. (b) Trace panels extracted from locations A, B, and C marked in (a) each show three traces: (1) true model with full elastic physics (solid black; True Model Elastic); (2) true model with acoustic approximation (dashed black; True Model Acoustic); and (3) inverted long-wavelength V_S model from starting Model C with elastic physics (solid red; Inverted Model Elastic).

5 Discussion

The numerical experiments presented above demonstrate several robust and interlinked findings about the sensitivity of low-frequency Scholte-waves, the practical value of multi-modal information, and the effectiveness of staged frequency-stepping strategies for estimating long-wavelength V_S structure in salt-bearing offshore settings. Below, we summarize the main observations, discuss their implications for offshore velocity model building and E-FWI, outline limitations and uncertainties, and identify the developments needed to advance toward field-ready applications using ambient seismic data.

5.1 Choice and construction of the starting model

The misfit-kernel analyses confirm that Scholte-wave tomography is dominated by V_S sensitivity (Figures 6–7). Scholte waves are P–SV coupled at the fluid–solid interface: while their phase velocities depend primarily on V_S, variations in V_P and ρ influence P–SV coupling, local impedance contrasts, and the effective elastic moduli. Because V_P and ρ are only weakly constrained by surface-wave travel times, inaccurate values can introduce parameter trade-offs and vertical smearing. Reliable V_P and ρ estimates—derived from active-source FWI, body-wave tomography, or empirical V_P–ρ relations—are therefore important to stabilize tomographic inversion and suppress crosstalk.

The comparative inversions using Models A and C support these conclusions. Even when all parameters were initialized from the background (Model A), the inversion successfully recovered the overall salt geometry and intermediate-depth V_S structure, demonstrating the strong intrinsic sensitivity of Scholte-wave travel times to V_S. However, the absence of true V_P and ρ contrasts introduced localized high-V_S artifacts beneath the salt, which diminished when the correct V_P–ρ distributions were used (Model C). These results highlight that accurate V_P–ρ priors primarily improve depth focusing and mitigate parameter trade-offs, rather than fundamentally changing the inversion's ability to recover large-scale salt geometry.

In practice, when reliable V_P and ρ models are available from body-wave FWI or reflection tomography, they should be used during Scholte-wave tomographic inversion, allowing the workflow to focus on recovering the long-wavelength V_S field. Where such constraints are unavailable, smooth background V_P and ρ models can still yield geologically consistent V_S recovery, particularly for lateral structure. For the initial V_S model, a practical approach would be to generate 1-D V_S profiles from MASW on ambient cross-correlations [e.g., 41], calibrate them using any available well, refraction, or empirical V_P–V_S relations, and interpolate them into a smooth 3-D background for initializing multimodal surface-wave adjoint tomography.

5.2 Tomographic inversion strategy and resolution

A hierarchical, frequency-stepped tomographic inversion that combines fundamental and higher-order modes mitigates cycle skipping, enhances depth coverage, and ensures stable convergence. The fundamental modes provide broad, shallow updates, whereas higher modes extend sensitivity to greater depths. This broad depth reach explains why the travel-time-adjoint workflow can recover long-wavelength salt geometry even when the starting model contains large (approximately 50%) V_S perturbations. Mode-specific refinement during the later stages (as seen in the staged S-1→S-4 sequence in our experiments) introduces finer structural details. Nevertheless, the effective vertical resolution is constrained by the available frequency band; as a result, the very shallow and deep intervals remain underresolved. These bandwidth limitations imply that the recoverable vertical extent of structure is directly governed by the available data frequency content.

5.3 Limitations, nonlinearity, and uncertainty

The numerical experiments presented here use 2-D synthetic EGFs with controlled preprocessing; field ambient cross-correlations will include non-ideal source distributions, cross-mode contamination, amplitude distortions from processing, and fully 3-D propagation effects that can bias tomographic kernels. The pseudo-Hessian preconditioner and spatial smoothing employed here are stabilizing approximations that require careful tuning for complex 3-D media. We also observe polarity reversals and cycle-skipping at higher frequencies (near 0.3 Hz for the fundamental mode), underscoring the inversion's nonlinearity and the need for judicious frequency scheduling and diagnostic evaluation at each stage.

5.4 Supporting field data observations

As noted in the Introduction, field VSG observations of Scholte-wave sensitivity motivated this study and its potential for constructing long-wavelength V_S models. Field VSGs from the Gulf of Mexico reported by [21]—reproduced in Figure 21 and Figure 22—provide empirical support for the main findings of this work. Figure 21 shows vertical–vertical ($\mathcal{C}_{zz}$) and radial–radial ($\mathcal{C}_{rr}$) component VSGs (left panels) together with their corresponding phase-velocity dispersion panels (right panels). The $\mathcal{C}_{zz}$ component is dominated by fundamental-mode Scholte energy (S_c^0), whereas the $\mathcal{C}_{rr}$ component exhibits strong higher-order modes (S_c^1 and S_c^2). In these dispersion panels, distinct fundamental and higher-order Scholte branches occupy the ambient band (∼0.1–0.6 Hz), similar to the frequency range exploited in this study.

Figure 22 presents snapshots extracted from a radial–radial ($\mathcal{C}_{rr}$) component VSG volume, illustrating first- and second-order Scholte-mode wavefronts (S_c^1 and S_c^2) propagating faster through the interpreted salt bodies (shown in pink, approximately 0.7 km beneath the mudline) than through the surrounding

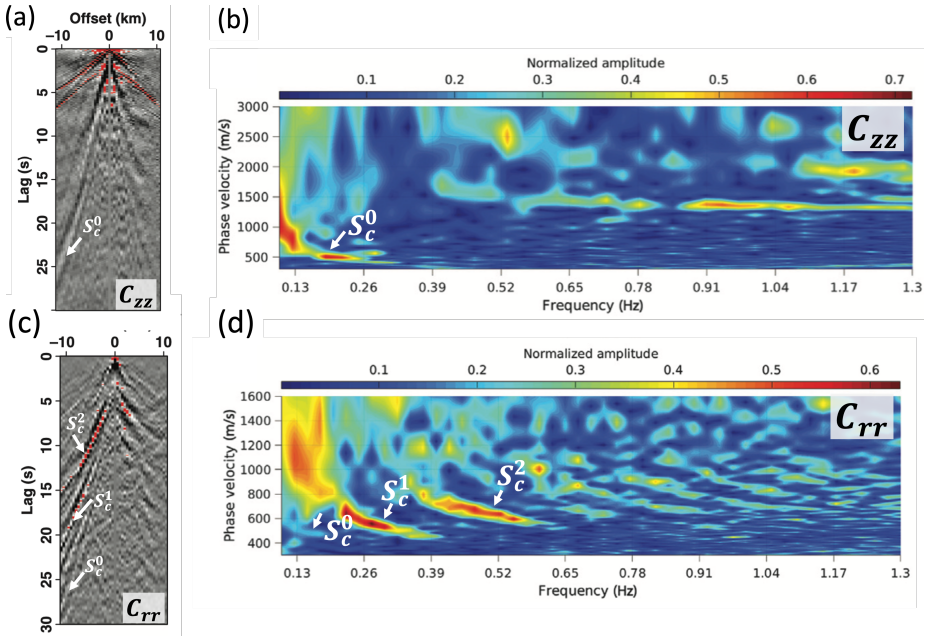

Fig. 21: Vertical–vertical ($\mathcal{C}_{zz}$) and radial–radial ($\mathcal{C}_{rr}$) component VSGs (left panels) and their corresponding phase-velocity dispersion panels (right panels) presented in [21]. Panels (a–b) show the $\mathcal{C}_{zz}$ component, and panels (c–d) show the $\mathcal{C}_{rr}$ component. S_c^0, S_c^1, and S_c^2 respectively denote the fundamental, first-, and second-order Scholte modes. Figure modified from Figures 5, 7, and 9 of [21].

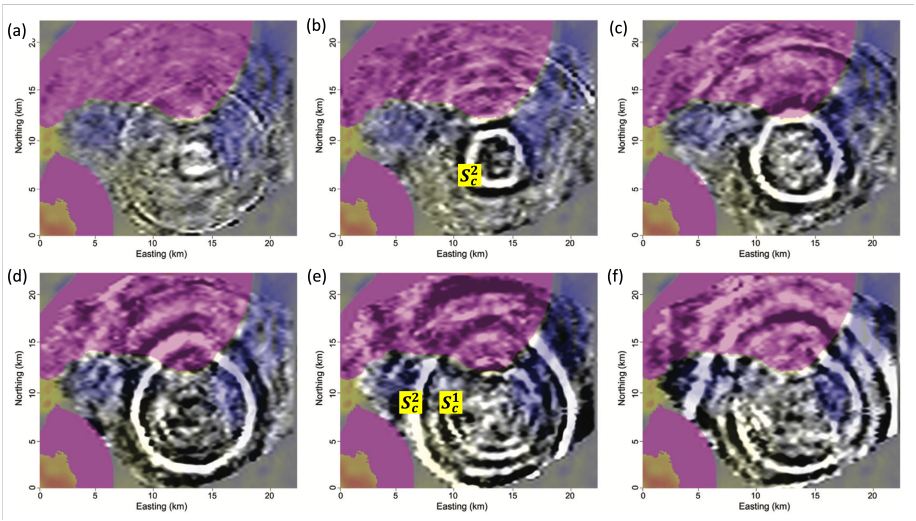

Fig. 22: Snapshots extracted from a radial-radial component ($\mathcal{C}_{rr}$), 0.3-0.8 Hz band VSG volume calculated near the center of the Gulf of Mexico OBN array presented in [21], shown at six propagation lags: (a) 5.0 s, (b) 7.0 s, (c) 9.0 s, (d) 11.0 s, (e) 13.0 s, and (f) 15.0 s. The illustrated wavefields have been overlain by the salt bodies (the pink) interpreted at a depth of 0.7 km from mudline. S_c^1 and S_c^2 denote the first- and second-order Scholte-mode wavefronts. Panels (d)–(f) clearly show Scholte waves propagating faster through the salt compared to those traveling within the surrounding clastic sediments. Figure taken and modified from Fig. 10 of [21].

clastics. Taken together, these field observations lend empirical support to two central claims of this work. First, low-frequency Scholte energy carries information about large-scale, long-wavelength V_S contrasts (e.g., salt versus sediment) through modal kinematics and partitioning—sensitivities that the multi-modal, frequency-stepped adjoint tomography developed here effectively exploits. Second, the differential modal expression between tensor components—$\mathcal{C}_{rr}$ emphasizing higher-order modes and $\mathcal{C}_{zz}$ emphasizing the fundamental mode, an observation also supported by cross-correlation modeling in [44]—underscores the importance of tensor-component-aware preprocessing and weighting during inversion to maximize vertical sampling and robustness. These field data therefore motivate a hierarchical inversion approach that combines fundamental and higher-order modes to extend depth sensitivity and stabilize convergence.

That said, the VSGs of [21] are cross-correlation products—not controlled active-source EGFs—and thus inherit the aforementioned real-world data complexities described earlier: non-uniform source illumination, amplitude distortions from processing, potential cross-mode contamination, and 3-D propagation effects. Because the observed Scholte-wave signatures arise in ambient cross-correlations rather than controlled shots (as active sources generally fail to

generate energy in this sub-1 Hz band), these observations justify treating ambient cross-correlations as self-consistent observables (not strict EGFs) in forward and inverse modeling, and emphasize the need to develop joint source–structure inversion strategies and full 3-D implementations before applying the workflow to field datasets.

5.5 Future work

Building on the sensitivities and inversion behavior demonstrated here, advancing Scholte-wave tomography toward field-ready application using ambient-seismic OBN data will require: (1) fully 3-D implementations; (2) joint inversion formulations that explicitly account for ambient source distributions and subsurface elastic structure rather than rely on EGF approximations; and (3) extensive real-data testing with tensor-aware preprocessing. Recent ambient modeling frameworks provide a practical and starting foundation for these developments [e.g., 43, 44], and—combined with the field VSG observations discussed above—point the way toward constructing long-wavelength V_S background models suitable as physically consistent starting input to active-source elastic FWI analyses.

6 Conclusions

Low-frequency Scholte-wave travel-time adjoint tomography provides an effective means of recovering the long-wavelength offshore shear-wave structure needed to initialize elastic full-waveform inversion. Our synthetic experiments lead to four principal conclusions. First, the misfit-kernel analyses confirm that Scholte waves are overwhelmingly sensitive to V_S variations, with only weak indirect dependence on V_P and ρ through Poisson's ratio and elastic moduli. This dominant V_S sensitivity was also reflected in the inversion results: even when all parameters were initialized from the background (Model A), the workflow successfully recovered the overall salt geometry and intermediate-depth V_S structure, demonstrating that large-scale V_S perturbation recovery is achievable without the true V_P and ρ contrasts. Second, introducing realistic V_P and ρ distributions (Model C) primarily improves depth focusing and reduces parameter trade-offs, mitigating the spurious high-V_S artifacts observed beneath the salt in the background-only case. Thus, accurate V_P–ρ priors—derived from active-source FWI, body-wave tomography, or empirical relations—enhance vertical resolution but are not strictly required for capturing the dominant lateral geometry of the salt. Third, lower-frequency and higher-order Scholte modes penetrate substantially deeper than higher-frequency fundamental-mode energy and are therefore essential for constraining long-wavelength deep structure. Combining fundamental and higher modes in a staged, frequency-stepped inversion improves both depth coverage and robustness: fundamental modes capture broad background updates, while higher modes contribute sharper structural detail. Finally, amplitude tests confirm that elastic forward modeling using the recov-

ered V_S reproduces converted-phase amplitudes that cannot be explained by an acoustic approximation, underscoring the importance of a physically consistent elastic background for subsequent high-frequency elastic FWI and joint inversion.

For practical applications, these findings motivate the acquisition and use of broader-band datasets to better resolve the shallowest and deepest structures, the development of joint inversion strategies for ambient datasets that explicitly account for both the ambient source distribution and the Earth's elastic structure, and the extension of the workflow to fully 3-D implementations and field OBN data. Overall, Scholte-wave adjoint travel-time tomography offers a promising approach for constructing robust low-frequency shear-wave velocity models, providing the critical foundation for improved high-frequency elastic FWI using active-source seismic data volumes.

References

[1] Keiiti Aki and Paul G. Richards. *Quantitative seismology*. University Science Books, 2 edition, 2002.

[2] GN Antonovskaya, ER Morozova, Ya V Konechnaya, and KB Danilov. Assessment of the Recording Capabilities of the Kolba Seismic Station for Seismic Monitoring in the Western Sector of the Russian Arctic. *Seismic Instruments*, 58(Suppl 2):S281–S290, 2022.

[3] Fabrice Ardhuin, Lucia Gualtieri, and Eléonore Stutzmann. How ocean waves rock the Earth: Two mechanisms explain microseisms with periods 3 to 300 s. *Geophysical Research Letters*, 42(3):765–772, 2015.

[4] Ebru Bozdağ, Jeannot Trampert, and Jeroen Tromp. Misfit functions for full waveform inversion based on instantaneous phase and envelope measurements. *Geophysical Journal International*, 185(2):845–870, 2011.

[5] Romain Brossier, Stéphane Operto, and Jean Virieux. Seismic imaging of complex onshore structures by 2D elastic frequency-domain full-waveform inversion. *Geophysics*, 74:WCC105–WCC118, 2009.

[6] Carey Bunks, Fatimetou M Saleck, Stephane Zaleski, and Guy Chavent. Multiscale seismic waveform inversion. *Geophysics*, 60(5):1457–1473, 1995.

[7] Sascha Bussat and Simone Kugler. Offshore ambient-noise surface-wave tomography above 0.1 Hz and its applications. *The Leading Edge*, 30(5):514–524, 2011.

[8] José M Carcione and Hans B Helle. The physics and simulation of wave propagation at the ocean bottom. *Geophysics*, 69(3):825–839, 2004.

[9] Hua-You Chai, Yu-Jun Cui, and Chang-Fu Wei. A parametric study of effective phase velocity of surface waves in layered media. *Computers and Geotechnics*, 44:176–184, 2012.

[10] Feng Cheng, Benxin Chi, Nathaniel J Lindsey, T Craig Dawe, and Jonathan B Ajo-Franklin. Utilizing distributed acoustic sensing and ocean bottom fiber optic cables for submarine structural characterization. *Scientific Reports*, 11(1):5613, 2021.

[11] Bryant Chow, Yoshihiro Kaneko, Carl Tape, Ryan Modrak, and John Townend. An automated workflow for adjoint tomography—waveform misfits and synthetic inversions for the North Island, New Zealand. *Geophysical Journal International*, 223(3):1461–1480, 2020.

[12] SAL de Ridder, BL Biondi, and RG Clapp. Time-lapse seismic noise correlation tomography at Valhall. *Geophysical Research Letters*, 41(17):6116–6122, 2014.

[13] Sjoerd de Ridder and Joe Dellinger. Ambient seismic noise eikonal tomography for near-surface imaging at Valhall. *The Leading Edge*, 30(5):506–512, 2011.

[14] Joseph Dellinger, Allan Ross, David Meaux, Andrew Brenders, Glenn Gesoff, John Etgen, John Naranjo, Graham Openshaw, and Mark Harper. Wolfspar®, an "FWI-friendly" ultralow-frequency marine seismic source. In *SEG International Exposition and Annual Meeting*, pages SEG–2016. SEG, 2016.

[15] Shuyuan Du, Jingpu Cao, Shihong Zhou, Yubo Qi, Lei Jiang, Yongfeng Zhang, and Changcheng Qiao. Observation and inversion of very-low-frequency seismo-acoustic fields in the South China sea. *The Journal of the Acoustical Society of America*, 148(6):3992–4001, 2020.

[16] Göran Ekström. A global model of Love and Rayleigh surface wave dispersion and anisotropy, 25-250 s. *Geophysical Journal International*, 187(3):1668–1686, 2011.

[17] Andreas Fichtner. *Full seismic waveform modelling and inversion*. Springer Science & Business Media, 2010.

[18] Andreas Fichtner, H-P Bunge, and Heiner Igel. The adjoint method in seismology: I. Theory. *Physics of the Earth and Planetary Interiors*, 157(1-2):86–104, 2006.

[19] Andreas Fichtner, Laurent Stehly, Laura Ermert, and Christian Boehm. Generalised interferometry-I. Theory for inter-station correlations. *Geophysical Journal International*, page ggw420, 2016.

[20] Aaron Girard, Jeffrey Shragge, Mike Danilochkine, Carsten Udengaard, and Sijmen Gerritsen. Observations from the Seafloor: Ultra-low-frequency Ambient Ocean-Bottom Nodal Seismology at the Amendment Field. *Geophysical Journal International*, 239(1):17–36, 07 2024.

[21] Aaron J Girard, Jeffrey Shragge, and Bjorn Olofsson. Low-frequency ambient ocean-bottom node surface-wave seismology: A Gulf of Mexico case history. *Geophysics*, 88(1):B21–B32, 2023.

[22] David Halliday and Andrew Curtis. Seismic interferometry, surface waves and source distribution. *Geophysical Journal International*, 175(3):1067–1087, 2008.

[23] Edwin L Hamilton. Shear-wave velocity versus depth in marine sediments: A review. *The Log Analyst*, 18(01), 1977.

[24] Klaus Hasselmann. A statistical analysis of the generation of microseisms. *Reviews of Geophysics*, 1(2):177–210, 1963.

[25] Brian Kennett. *Seismic wave propagation in stratified media*. ANU Press, 2009.

[26] WP Kimman and J Trampert. Approximations in seismic interferometry and their effects on surface waves. *Geophysical Journal International*, 182(1):461–476, 2010.

[27] Dimitri Komatitsch, Christophe Barnes, and Jeroen Tromp. Wave propagation near a fluid-solid interface: A spectral-element approach. *Geophysics*, 65(2):623–631, 2000.

[28] Dimitri Komatitsch and Jeroen Tromp. Spectral-element simulations of global seismic wave propagation—I. Validation. *Geophysical Journal International*, 149(2):390–412, 2002.

[29] Bogdan Kustowski, G Ekström, and AM Dziewoński. The shear-wave velocity structure in the upper mantle beneath Eurasia. *Geophysical Journal International*, 174(3):978–992, 2008.

[30] Myung W Lee. Comparison of methods for predicting shear-wave velocities of unconsolidated shallow sediments in the Gulf of Mexico. Technical report, US Geological Survey, 2013.

[31] Dong C Liu and Jorge Nocedal. On the limited memory BFGS method for large scale optimization. *Mathematical Programming*, 45(1):503–528, 1989.

[32] Q Liu and YJ Gu. Seismic imaging: From classical to adjoint tomography. *Tectonophysics*, 566:31–66, 2012.

[33] Qinya Liu and Jeroen Tromp. Finite-frequency kernels based on adjoint methods. *Bulletin of the Seismological Society of America*, 96(6):2383–2397, 2006.

[34] Qinya Liu and Jeroen Tromp. Finite-frequency sensitivity kernels for global seismic wave propagation based upon adjoint methods. *Geophysical Journal International*, 174(1):265–286, 2008.

[35] Michael Selwyn Longuet-Higgins. A theory of the origin of microseisms. *Philosophical Transactions of the Royal Society of London. Series A, Mathematical and Physical Sciences*, 243(857):1–35, 1950.

[36] Alessia Maggi, Carl Tape, Min Chen, Daniel Chao, and Jeroen Tromp. An automated time-window selection algorithm for seismic tomography. *Geophysical Journal International*, 178(1):257–281, 2009.

[37] Jian Mao, Ru-Shan Wu, and Baoli Wang. Multiscale full waveform inversion using GPU. In *SEG Technical Program Expanded Abstracts 2012*, pages 1–7. Society of Exploration Geophysicists, 2012.

[38] Ryan Modrak and Jeroen Tromp. Seismic waveform inversion best practices: regional, global and exploration test cases. *Geophysical Journal International*, 206(3):1864–1889, 2016.

[39] Ryan T Modrak, Dmitry Borisov, Matthieu Lefebvre, and Jeroen Tromp. Seisflows—Flexible waveform inversion software. *Computers & Geosciences*, 115:88–95, 2018.

[40] A Mordret, M Landès, NM Shapiro, SC Singh, P Roux, and OI Barkved. Near-surface study at the Valhall oil field from ambient noise surface wave tomography. *Geophysical Journal International*, 193(3):1627–1643, 2013.

[41] Ivan Lim Chen Ning, Justin Tan, and Ranjan Dash. Sparse ocean-bottom node seismic interferometry and inversion: A Gulf of Mexico study. In *Fourth International Meeting for Applied Geoscience & Energy*, pages 1830–1834. Society of Exploration Geophysicists and American Association of Petroleum Geologists, 2024.

[42] Jorge Nocedal and Stephen J Wright. *Numerical optimization*. Springer, 2006.

[43] Adesh Pandey, Sjoerd de Ridder, Jeffrey Shragge, and Aaron J. Girard. Ocean-bottom seismic interferometry in coupled acoustic-elastic media. *Geophysical Journal International*, 242(3):ggaf271, 2025.

[44] Adesh Pandey, Jeffrey Shragge, and Aaron J. Girard. First-order Control Factors for Ocean-bottom Ambient Seismology Interferometric Observations. *Geophysical Journal International*, 243(2):ggf351, 2025.

[45] Choon B Park, Richard D Miller, and Jianghai Xia. Multichannel analysis of surface waves. *Geophysics*, 64(3):800–808, 1999.

[46] Michael H Ritzwoller and Anatoli L Levshin. Estimating shallow shear velocities with marine multicomponent seismic data. *Geophysics*, 67(6):1991–2004, 2002.

[47] Korbinian Sager, Christian Boehm, Laura Ermert, Lion Krischer, and Andreas Fichtner. Global-scale full-waveform ambient noise inversion. *Journal of Geophysical Research: Solid Earth*, 125(4):e2019JB018644, 2020.

[48] Korbinian Sager, Laura Ermert, Christian Boehm, and Andreas Fichtner. Towards full waveform ambient noise inversion. *Geophysical Journal International*, 212(1):566–590, 2018.

[49] Caiwang Shi, Hengxin Ren, and Xiaofei Chen. Dispersion inversion for P-and S-wave velocities based on guided P and Scholte waves. *Geophysics*, 88:R721–R736, 2023.

[50] Laurent Sirgue and R Gerhard Pratt. Efficient waveform inversion and imaging: A strategy for selecting temporal frequencies. *Geophysics*, 69(1):231–248, 2004.

[51] Zack J Spica, Jorge C Castellanos, Loïc Viens, Kiwamu Nishida, Takeshi Akuhara, Masanao Shinohara, and Tomoaki Yamada. Subsurface imaging with ocean-bottom distributed acoustic sensing and water phases reverberations. *Geophysical Research Letters*, 49(2):e2021GL095287, 2022.

[52] Peter Stewart. Interferometric imaging of ocean bottom noise. In *SEG International Exposition and Annual Meeting*, pages 1555–1559. SEG, 2006.

[53] George H Sutton and Noël Barstow. Ocean-bottom ultralow-frequency (ULF) seismo-acoustic ambient noise: 0.002 to 0.4 Hz. *The Journal of the Acoustical Society of America*, 87(5):2005–2012, 1990.

[54] Carl Tape, Qinya Liu, Alessia Maggi, and Jeroen Tromp. Seismic tomography of the southern California crust based on spectral-element and adjoint methods. *Geophysical Journal International*, 180(1):433–462, 2010.

[55] Carl Tape, Qinya Liu, and Jeroen Tromp. Finite-frequency tomography using adjoint methods—Methodology and examples using membrane surface waves. *Geophysical Journal International*, 168(3):1105–1129, 2007.

[56] Albert Tarantola. *Inverse problem theory and methods for model parameter estimation*. SIAM, 2005.

[57] Jeroen Tromp, Carl Tape, and Qinya Liu. Seismic tomography, adjoint methods, time reversal and banana-doughnut kernels. *Geophysical Journal International*, 160(1):195–216, 2005.

[58] Jean Virieux and Stéphane Operto. An overview of full-waveform inversion in exploration geophysics. *Geophysics*, 74:WCC1–WCC26, 2009.

[59] Kai Wang, Yingjie Yang, Piero Basini, Ping Tong, Carl Tape, and Qinya Liu. Refined crustal and uppermost mantle structure of southern California by ambient noise adjoint tomography. *Geophysical Journal International*, 215(2):844–863, 2018.

[60] Yuan Wang, Zhiwei Li, Jianhua Geng, Qingyu You, Tianyao Hao, Yaoxing Hu, Chunlei Zhao, Yan Zhang, and Yuzhu Liu. Seismic imaging of S-wave structures of shallow sediments in the East China sea using OBN multicomponent Scholte-wave data. *Geophysics*, 85:EN87–EN104, 2020.

[61] Yuan Wang, Qingyu You, and Tianyao Hao. Estimating the shear-wave velocities of shallow sediments in the Yellow Sea using ocean-bottom-seismometer multicomponent Scholte-wave data. *Frontiers in Earth Science*, 10:812744, 2022.

[62] K Wapenaar. Retrieving the elastdynamic Green's function of an arbitrary inhomogeneous medium by cross correlation. *Physical Review Letters*, 93(254301):1–4, 2004.

[63] Jianghai Xia. Estimation of near-surface shear-wave velocities and quality factors using multichannel analysis of surface-wave methods. *Journal of Applied Geophysics*, 103:140–151, 2014.

[64] Jianghai Xia, Richard D Miller, Choon B Park, and Gang Tian. Inversion of high frequency surface waves with fundamental and higher modes. *Journal of Applied Geophysics*, 52(1):45–57, 2003.

[65] Zongbo Xu, T Dylan Mikesell, Gabriel Gribler, and Aurélien Mordret. Rayleigh-wave multicomponent cross-correlation-based source strength distribution inversion. Part 1: Theory and numerical examples. *Geophysical Journal International*, 218(3):1761–1780, 2019.

[66] Yanhua O Yuan, Ebru Bozdağ, Caio Ciardelli, Fuchun Gao, and Frederik J Simons. The exponentiated phase measurement, and objective-function hybridization for adjoint waveform tomography. *Geophysical Journal International*, 221(2):1145–1164, 2020.

[67] Hejun Zhu, Ebru Bozdağ, and Jeroen Tromp. Seismic structure of the European upper mantle based on adjoint tomography. *Geophysical Journal International*, 201(1):18–52, 2015.